



Recent advances in optoelectronic and microelectronic devices based on ultrawide-bandgap semiconductors



Jialin Yang ^a, Kewei Liu ^{a,b,*}, Xing Chen ^{a,b}, Dezhen Shen ^{a,b,**}

^a State Key Laboratory of Luminescence and Applications, Changchun Institute of Optics, Fine Mechanics and Physics, Chinese Academy of Sciences, Changchun, 130033, PR China

^b Center of Materials Science and Optoelectronics Engineering, University of Chinese Academy of Sciences, Beijing, 100049, PR China

ABSTRACT

Owing to their novel physical properties, semiconductors have penetrated almost every corner of the contemporary industrial system. Nowadays, semiconductor materials and their microelectronic and optoelectronic devices are widely used in civil and military fields. Recently, ultrawide-bandgap (UWBG) semiconductors with bandgaps considerably wider than 3.4 eV of GaN, such as aluminium gallium nitride (AlGaN), gallium oxide (Ga_2O_3), and diamond, have attracted increasing attention due to their advantages, including high breakdown field, high stability, and high radiation resistance. In this review, recent research pertaining to UWBG semiconductors in optoelectronics and microelectronics is introduced. Moreover, the challenges and opportunities of UWBG semiconductors are deliberated. It is expected that this review will provide inspiration and insights for further related research.

1. Introduction

Semiconductors, with the conductivity lying between conductors and insulators, have been essential for the development of modern science and technology. Since the invention of the first transistor in the 1930s [1], semiconductor materials and related technologies have brought revolutionary changes. Semiconductor materials have been through three stages of development. The first generation of semiconductor materials (e.g., Si and Ge) promoted the rapid development of the microelectronics industry centred on integrated circuits. The second generation semiconductors (e.g. GaAs and InP) have important applications in the fields of red/infrared optoelectronics and high-speed microelectronics. With the wide bandgap, high breakdown field, excellent thermal/chemical stability, the third generation semiconductors (also called wide-bandgap (WBG) semiconductors) (GaN, SiC, ZnO, etc.) have occupied a central position in the fields of blue/ultraviolet (UV) optoelectronic devices, and high-power and high-frequency microelectronic devices. Typically, GaN-based blue/UV light-emitting diodes (LEDs) have led to a revolution in the lighting industry. The scientists who invented these LEDs were awarded the Nobel Prize in Physics in 2014. These three generations of semiconductors have their own advantages and suitable device applications, and they can coexist and complement each other for a long time. Nowadays, semiconductor materials and technologies are considered the cornerstone of the modern information society, which have already penetrated every corner of the contemporary industrial system.

With the development of modern science and technology, the demand for optoelectronic devices with short wavelengths and microelectronic devices with high power and frequency is increasing. In recent years, ultrawide-bandgap (UWBG) semiconductors, with

* Corresponding author. State Key Laboratory of Luminescence and Applications, Changchun Institute of Optics, Fine Mechanics and Physics, Chinese Academy of Sciences, Changchun, 130033, PR China.

** Corresponding author. State Key Laboratory of Luminescence and Applications, Changchun Institute of Optics, Fine Mechanics and Physics, Chinese Academy of Sciences, Changchun, 130033, PR China.

E-mail addresses: liukw@ciomp.ac.cn (K. Liu), shendz@ciomp.ac.cn (D. Shen).

bandgap of considerably wider than 3.4 eV of GaN, have attracted increasing attention due to their promising optical and electrical properties. UWBG semiconductors such as AlGaN, diamond, and Ga_2O_3 (as shown in Fig. 1(a)) have a wider bandgap, higher breakdown field, and stronger stability and radiation hardness than WBG semiconductors. Therefore, UWBG semiconductors show broad and considerable application prospects in UV luminescence, UV laser, UV detection, and high-power and high-frequency devices (as shown in Fig. 1(b)).

Optical bandgap (E_g) can be calculated using the following equation:

$$E_g = \frac{hc}{\lambda} \quad (1)$$

where λ is the wavelength, h is the Planck constant, and c is the speed of light. Considering that bandgaps of UWBG semiconductors are considerably wider than 3.4 eV, their optoelectronic devices could be operated with the wavelength much shorter than 365 nm. These devices have many special applications. In particular, UVC (200–280 nm) emitting devices based on UWBG semiconductors have considerable development potential for applications such as chemical-free disinfection, lithography, medicine, and micromachining. UVC photodetectors (known as ‘solar-blind’ photodetectors because UVC radiations from the sun are strongly absorbed by the ozone layer and cannot reach the ground) have important application prospects in various military and civilian fields, including flame warning, confidential communication, and missile alerting.

Furthermore, because of the excellent electrical properties of UWBG semiconductors, they have great application potential in microelectronics. Three figure-of-merits (FOMs) have been proposed to quantify the suitability of semiconductor materials for micro-electronic applications, namely, Johnson's FOM (JFOM), Keyes' FOM (KFOM), and Baliga's FOM (BFOM) [2–5]. JFOM is used to evaluate the suitability of semiconductor materials in high-frequency power devices, which is defined as [3]:

$$JFOM = \frac{E_b \cdot v_s}{2\pi} \quad (2)$$

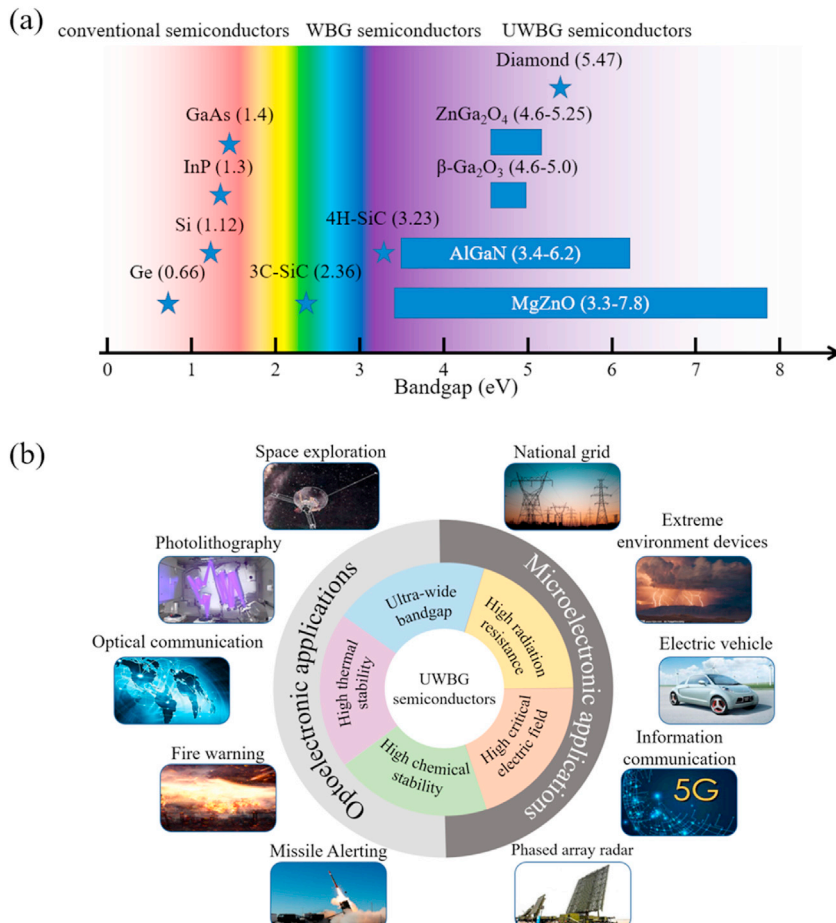


Fig. 1. (a) Bandgap energies of various semiconductors. (b) Characteristics and applications of UWBG semiconductor materials.

where E_b is the breakdown field, and v_s is the saturated drift velocity. KFOM is used to evaluate the thermal limitation of the switching behaviour of the semiconductor microelectronic devices, which is defined as [4]:

$$KFOM = \sigma_{thermal} \cdot \left(\frac{c \cdot v_s}{4\pi\epsilon} \right)^{\frac{1}{2}} \quad (3)$$

where $\sigma_{thermal}$ is the thermal conductivity, c is the velocity of light in free space, and ϵ is the relative permittivity. BFOM is used to evaluate the suitability of semiconductor materials in low-frequency and high-power devices, which is defined as [5]:

$$BFOM = \epsilon \mu E_b^3 \quad (4)$$

where μ is the carrier mobility. The FOMs of some semiconductors are summarised in Table 1. For comparison, the FOMs are normalised by Si. JFOM and BFOM are strongly dependent on the breakdown field, which indicates that UWBG semiconductors have considerable advantages in the application of high-power and high-frequency devices. Combined with their high thermal stability, high chemical stability, and high radiation resistance, these UWBG semiconductors are considered essential candidate materials in microelectronic fields such as state grid, electric vehicles, information communication, and phased array radar, including extreme environmental devices in future.

Till now, the research on UWBG semiconductors has achieved great progress and rapid development. Several review articles have summarised some developments related to UWBG semiconductor materials. Tsao et al. discussed the opportunities and challenges faced by UWBG semiconductors in applications [20]. Xie et al. presented the research progress of UWBG semiconductor-based UV photodetectors [21]. In view of the important application value of UWBG semiconductor materials and their electronic devices, it is necessary to systematically and comprehensively summarise the research progress of UWBG semiconductor-based optoelectronic and microelectronic devices. Therefore, in this paper, first, we briefly introduce some performance parameters involved in optoelectronic and microelectronic devices. Then, recent research pertaining to UWBG semiconductor-based optoelectronic and microelectronic devices is systematically introduced according to materials used. Finally, challenges and opportunities in application of UWBG semiconductors are deliberated, and future scope in the development of UWBG semiconductor materials is presented. This review provides inspiration and insights for future research on UWBG semiconductors.

2. Performance parameters

Semiconductor-based optoelectronic devices include LEDs, laser diodes (LDs), and photodetectors, and semiconductor-based microelectronic devices include power devices and radio frequency (RF)/microwave devices. Each device has specific parameters for quantifying its performance. This section briefly introduces some of these performance parameters.

2.1. Optoelectronic devices

2.1.1. Light-emitting and laser diodes

In general, both the LEDs and LDs are p–n junction diodes made from semiconductors. For LEDs, under forward-biased condition, the holes and the electrons from the p- and n-type layers, respectively, recombine each other in an active region to emit spontaneous radiation, whereas for LDs, an additional optical resonator structure must be designed and fabricated for the active region. When adequate forward bias voltage is applied to LDs, population inversion occurs in the active region. A small number of photons generated by spontaneous emission are reflected in the resonator, leading to the emission of stimulated radiation from the active region.

Quantum efficiency (QE, η) is a key parameter to quantify the performance of LEDs and LDs, and it can be classified into external QE (EQE) and internal QE (IQE). EQE η_{ext} is the ratio of the number of photons emitted into free space per unit time to the number of electrons injected into the device per unit time. IQE η_{int} is the ratio of the number of photons emitted per unit time from the active region

Table 1
Characteristic parameters of different semiconductor materials.

Materials	E_g (eV)	E_b (MV/ cm)	Mobility@ N_D or $N_A^a \geq 10^{16}\text{cm}^{-3}$ ($\text{cm}^2/(\text{V}\cdot\text{s})$)	saturation velocity ($\times 10^7$ cm/s)	ϵ	$\sigma_{thermal}$ (W/(m•K))	JFOM/Si	KFOM/Si	BFOM/ Si
Si [6]	1.12	0.3	1450 (electron) 1000 (electron) [8]	1.0 (electron) 2.9 (electron) [9]	11.9 10.4 [6]	159 230 [10] [11]	1	1	1
GaN	3.4	3 [7]	426 (electron) [12]	1.7 (electron) [9]	11.5 [11]	319 [13]	85	2.66	603
AlN	6.0	15 [11]	1370 (hole) [15]	1.9 (electron)/1.4 (hole) [16]	5.7 [6]	3450 (isotopically pure) [17]	63 (electron)/ 47 (hole)	2.66	35490
Diamond	5.5	10 [14]	300 (electron) [18]	2 (electron) [19]	10 [18]	27 [10]	53	43.22 (electron)/ 37.10(hole)	16762
β -Ga ₂ O ₃	4.9	8 [18]						0.26	3297

^a N_D and N_A are the donor and acceptor concentrations, respectively.

to the number of electrons injected into the device per unit time. The equations of EQE and IQE for LEDs (or LDs) are as follows:

$$\eta_{ext} = \frac{P(\lambda)/(hc/\lambda)}{I/e} \quad (5)$$

$$\eta_{int} = \frac{P_{int}(\lambda)/(hc/\lambda)}{I/e} \quad (6)$$

where $P(\lambda)$ is the optical output power emitted to the free space at wavelength of λ , $P_{int}(\lambda)$ is the optical power emitted from the active region at wavelength of λ , I is the input current, and e is the electronic charge. In general, the light generated by the active regions is scattered or absorbed in the device; thus, EQE η_{ext} and the IQE η_{int} are given using the following equation:

$$\eta_{ext} = \eta_{int} \times \eta_{extr} \quad (7)$$

where η_{extr} is the light-extraction efficiency (LEE).

In addition to QE, wall-plug efficiency (WPE) is also used to evaluate the optical performance of LEDs. It is defined as the ratio of the optical output power to the input electric power. The relationship between WPE and EQE is given as follows:

$$WPE = \frac{\eta_{ext}}{V} \times \frac{hc/\lambda}{e} \quad (8)$$

where V is the drive voltage of the LED.

For LDs, the threshold current density (J_{th}) is the minimum current density required to achieve lasing. The linewidth, that is, the half-height width (FWHM) of the LD emission peak, can be used to determine the monochromaticity of a laser.

2.1.2. Photodetectors

Photodetectors are a type of devices that convert optical signals into electrical signals by using the photoelectric effect. When the incident photon energy is higher than the bandgap of the semiconductor in the active region, the electrons can be excited and moved from the valence band to the conduction band, resulting in photogenerated electron-hole pairs. Driven by the built-in electric field or external electric field, the photogenerated electron-hole pairs are separated and move to the opposite direction, thereby generating an electrical signal.

For photodetectors, EQE is the ratio of the number of photoelectrons generated per unit time to the number of photons incident on the device. IQE is the ratio of the number of photoelectrons generated per unit time to the number of photons absorbed within the active region of the device. EQE and IQE for photodetectors are given as follows:

$$\eta_{ext} = \frac{I_{ph}/e}{P(\lambda)/(hc/\lambda)} \quad (9)$$

$$\eta_{int} = \frac{I_{ph}/e}{P_{int}(\lambda)/(hc/\lambda)} \quad (10)$$

where $P(\lambda)$ is the optical power incident on the device at wavelength of λ , $P_{int}(\lambda)$ is the optical power absorbed on the active region of the device at wavelength of λ , and I_{ph} is the output photocurrent. When most light incident on the device is collected by the active region, $\eta_{ext} \approx \eta_{int}$.

Generally, a photon with enough energy can excite only one photogenerated electron-hole pair collected as electrical signals, that is, $\eta \leq 1$. However, in practical experiments, the measured QE of some photodetectors is > 1 because of the gain mechanism in the devices. Therefore, gain plays an important role in photodetectors, especially in weak-signal detection.

Responsivity is an important parameter for evaluating the detection ability of photodetectors. It is defined as the ratio of the light power incident on the device to the output photocurrent. According to equation (9), the relationship between R and QE is given as follows:

$$R(\lambda) = \frac{I_{ph}}{P(\lambda)} = \eta_{ext} \frac{e}{hc/\lambda} \quad (11)$$

where the QE takes the gain into account.

High-performance photodetectors require high responsivity and low noise. Noise can come from the external or internal sources. The internal noise, including all noise generated within the device, should be as low as possible. Dark current, I_d , is the current in photodetectors in the absence of incident light. Generally, the dark current is a main source of internal noise for a photodetector.

Noise equivalent power (NEP) is an important parameter for photodetectors and characterises their sensitivity. It is defined as the incident light power required to produce a signal-to-noise ratio of 1. The smaller is the NEP, the better is the photodetector.

The detectivity (D) is another criterion used to evaluate the performance of the photodetector and is defined as the reciprocal of NEP. The larger is the detectivity of a photodetector, the more suitable it is for detecting weak light signals. The specific detectivity (D^*), also

known as normalised detectivity, is the detectivity normalised to a unit detector area and detection bandwidth. D^* can be expressed as follows:

$$D^* = D \sqrt{S \cdot \Delta f} = \frac{\sqrt{S \cdot \Delta f}}{NEP} \quad (12)$$

where S is the area of the photosensitive region of the detector, and Δf is the frequency bandwidth. The unit of D^* is Jones ($\text{cm Hz}^{1/2}/\text{W}$), in honour of R. Clark Jones, who originally defined it in the 1950s [22].

The response speed of a photodetector is an important parameter to promptly respond to a signal. The rise time (t_r) and fall time (t_f) are generally used to describe the speed of the photodetector. t_r and t_f are commonly defined as the time required for the signal to rise from 10% to 90% and fall from 90% to 10% of the final value, respectively. Shorter rise and fall times indicate faster response speed of the device.

2.2. Microelectronic devices

2.2.1. High-power devices

High-power devices are microelectronic devices that operate at high voltage and high current. The power devices mainly include two- and three-terminal devices. Two-terminal power devices have a simple structure, which is commonly based on p-n junction and Schottky junction. By utilising the unilateral conductivity of the junctions, two-terminal power devices can rectify the circuit. By contrast, three-terminal power devices are generally based on transistor structures. By adjusting the gate voltage, three-terminal power devices can switch the current in the circuit. In general, the breakdown voltage (V_b) determines the application limit of high-power devices. To minimise its heat loss, the specific on-resistance ($R_{on,sp}$) of a high-power device should be minimised. In addition, for a constant gate voltage, the drain saturation current density is inversely proportional to the specific on-resistance; thus, the drain saturation current density of high-power devices should be high.

Considering the two factors of V_b and $R_{on,sp}$, an FOM (PFOM) is proposed to quantify the performance of high-power devices [23,24]:

$$PFOM = \frac{V_b^2}{R_{on,sp}} \quad (13)$$

In addition, transistors can be divided into normally on (sometimes called depletion mode, D-mode) devices and normally off (sometimes called enhance mode, E-mode) devices according to the conduction state of their channel without gate bias. The threshold voltage (V_{th}) represents the gate bias voltage required when the transistor is turned on. For n-type unipolar transistors, when $V_{th} < 0$ (for p-type unipolar transistors, $V_{th} > 0$), it is a normally on device, and when $V_{th} > 0$ (for p-type unipolar transistors, $V_{th} < 0$), it is a normally off device. To ensure safety and stability, normally off devices are often considered more suitable for high-power devices.

2.2.2. Radio frequency (RF)/microwave devices

RF/microwave transistor amplifiers are a type of microelectronic devices working at high frequency. In general, a weak signal is applied to the input terminal (commonly the gate for a field-effect transistor), and an amplified signal appears at the output terminal (commonly the drain for a field-effect transistor). For these high-frequency transistor amplifiers, the cut-off frequency (f_T , operating frequency when the current gain decreases to 1) and maximum oscillation frequency (f_{max} , operating frequency when the maximum unilateral power gain decreases to 1) are important parameters for evaluating their performance. f_T and f_{max} determine the upper limit of the operating frequency of RF/microwave devices.

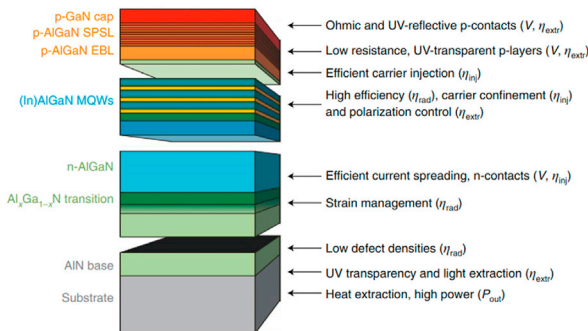


Fig. 2. Schematic diagram of the AlGaN-based LED device structure [25]. Reprinted by permission from [Springer Nature and Copyright Clearance Centre]: [Nature], [Nature Photonics], Ref [25], [copyright] (2019).

3. Optoelectronic and microelectronic applications

3.1. Aluminium gallium nitride (AlGaN)

AlGaN is a ternary alloy of GaN and AlN . By adjusting the ratio of Al and Ga, the bandgap can be adjusted from 3.4 eV for GaN to 6.2 eV for AlN . Over the past two decades, considerable achievements have been made in the research on AlGaN -based optoelectronic and microelectronic devices, which are summarised in this section.

3.1.1. AlGaN -based optoelectronic devices

3.1.1.1. AlGaN UV LEDs and LDs

Structure of AlGaN UV LEDs. As shown in Fig. 2, a typical structure of AlGaN -based LED comprises an AlN layer, an AlGaN transition layer, an n-type AlGaN layer, AlGaN multiple quantum wells (MQWs), an electron blocking layer (EBL), and p-type AlGaN and p-type GaN cap layers. The AlN layer on the substrate provides a high-quality template for the subsequent epitaxial growth of the device. The AlGaN transition layer could reduce the effects of lattice mismatch between the $\text{AlN}/\text{substrate}$ and the n-type AlGaN layer. The n-type layer serves as the electron injection layer. MQWs are the active regions of LED devices and are sandwiched by n-type and p-type AlGaN layers. They play an essential role in the IQE of devices. The EBL with a large barrier height could effectively improve the injection efficiency due to the suppression of overflow electrons above the MQWs into the p-type AlGaN layers. The p-type AlGaN layer is utilised as the hole injection layer. The heavily Mg-doped p-GaN cap layer acts as the p-type contact layer.

3.1.1.1.2. Design and optimisation of AlGaN UV LEDs to enhance their quantum efficiency

Improvement of LEE

The strong UV light absorption in the p-GaN contact layer is considered a main reason for the low LEE of AlGaN UV vertical LED. To improve the LEE of AlGaN UV LEDs, the introduction of a transparent p-AlGaN contact layer and highly reflective p-electrode is the most commonly used method [26–33]. Till now, various p-electrodes with high UV reflectance have been used in the reported AlGaN -based LEDs. Among them, Al electrodes are suitable for the p-type layer because of its high reflectivity (92%) in the UV band. However, it is difficult to form good Ohmic contact between an Al electrode and p-AlGaN with high Al content. To resolve this problem, Zhang et al. inserted a thin InGaN layer between the Al electrode and p-AlGaN to form a metal–semiconductor tunnelling junction [33], which improved the hole injection efficiency. Combined with the high reflectivity of the Al electrode, the EQE and WPE of the device are improved by 75% and 39%, respectively, compared with a device using an Ni electrode. Alternatively, Lee et al. reported a three-layer structure, p-AlGaN/Ni:AlN/Al [29]. The reflectivity of this structure was >90%. By using a pulsed electrical breakdown method, many conductive filaments were formed in Ni:AlN, leading to good Ohmic contact while the reflectivity remained unchanged. The EQE of the device at 283 nm was as high as 8.49%. In addition to the Al electrode, Ni/Mg and In electrodes are considered good candidates with reflectivities of 80% and 87%, respectively. Maeda et al. demonstrated AlGaN deep-UV (DUV) LED with a Ni/Mg electrode. The EQE of LED with the Ni/Mg electrode was higher by 60% than that with the Ni/Au electrode [32]. More recently, Guttmann et al. used In as the

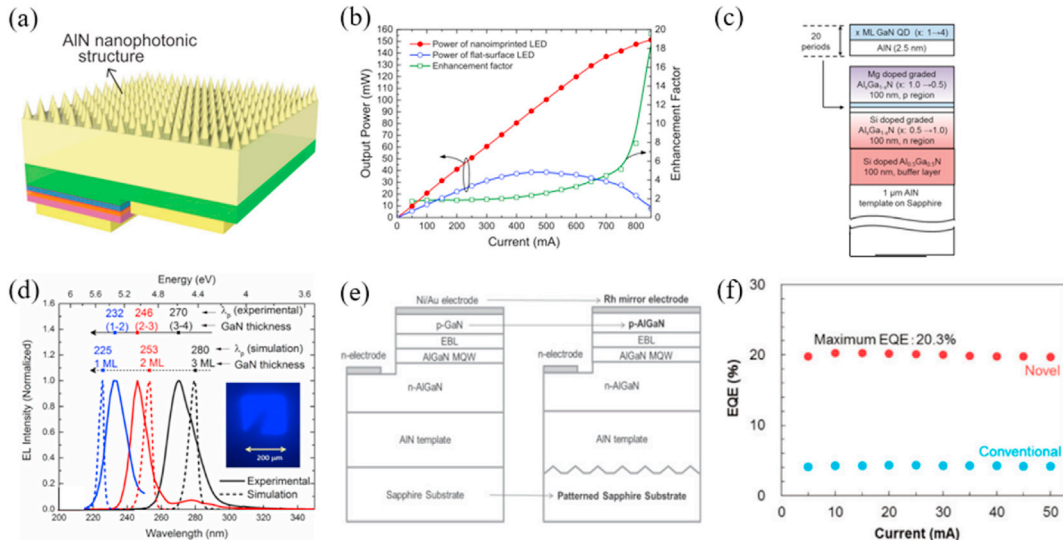


Fig. 3. (a) Schematic of the AlN nanophotonic light-extraction structure. (b) Output power and enhancement factor characteristics of LEDs with and without the nanophotonic structure [34]. Reprinted from Ref. [34], with the permission of AIP Publishing. (c) Device structure of AlN-delta-GaN MQWs LEDs. (d) Comparison between the measured and simulated electroluminescence spectra of AlN-delta-GaN MQWs LEDs [37]. Reprinted from Ref. [37], with the permission of AIP Publishing. (e) Schematics of conventional (left) and novel (right) of AlGaN -based LED structures. (f) EQE–current characteristics of the LED with conventional and novel structures [53]. Copyright (2017) The Japan Society of Applied Physics.

electrode of the p-type layer [27]. Compared with Au and Pd/Al/Au electrodes, the use of an In electrode significantly improved the values of LEE and EQE. In addition to selecting appropriate electrode materials, improving the reflectivity of the p-type layer is essential to enhance the LEE. Kashima et al. proposed a scheme for improving the reflectivity of the p-type layer by introducing the photonic crystal structure [28]. They fabricated air-hole type high-reflectivity photonic crystals on *p*-AlGaN surface via nanoimprinting and inductively coupled plasma dry-etching. By introducing high-reflectivity photonic crystals, the peak emission at 283 nm of the devices can reach 10%, which is 23% higher than that without photonic crystals. Liu et al. used p-Si as a hole injection layer and a UV reflector [30]. The EQE of the peak emission at 226 nm was as high as 0.2%.

Moreover, the fabrication of specific structures on the substrate can also achieve a high LEE. Inoue et al. used a nanoimprint lithography process to fabricate a nanophotonics light-extraction structure on the back of an AlN substrate (as shown Fig. 3(a)) [34]. Compared with the conventional flat-surface structure device, the AlGaN LED with nanostructured surface showed a significantly effective reduction in the efficiency droop under high current injection (Fig. 3(b)), and its output power at an injection current of 850 mA increased by nearly 20 times.

The output mode of MQWs also has a considerable influence on the LEE. Under the effect of crystal field and spin orbit coupling, the valence band top of AlGaN material splits into three sub-bands, namely a heavy hole (HH) band, a light hole (LH) band, and a crystal field split-off hole (CH) band [35]. For GaN and AlGaN with a low Al content, the HH and LH bands are above the CH band, and then the excited electrons preferentially transfer from the conduction band to the HH and LH bands, radiating light with the transverse electric mode (TE-mode, the electric field component of electromagnetic wave is perpendicular to the *c*-axis). With the increase in the Al content, the CH band rises above the HH and LH bands, light is mainly radiated in the transverse magnetic mode (TM-mode, part of the electric field component in the electromagnetic wave is parallel to the *c*-axis) [36]. In general, the *c*-axis of AlGaN crystal is parallel to the direction of the light emission in an AlGaN UV LEDs. Therefore, the LEE of high Al-content AlGaN LEDs could be reduced because of the great loss of TM-mode emission during propagation in the device. To solve this problem, an AlN-delta-GaN MQWs structure has been fabricated by Jena's group and Zhang's group as shown in Fig. 3(c) [37,38]. This structure considerably improves the spontaneous emission rate of the TE-mode. More interestingly, the emission wavelength of the corresponding LED can be tuned by adjusting the thickness of the GaN layer (Fig. 3(d)).

Improvement of IQE

Crystal quality is the most important factor affecting the IQE of AlGaN-based UV LEDs. Due to the lack of high-quality native substrates, the dislocations in AlGaN films are inevitably induced, which commonly degrade device performance [39]. In 2011, Ban et al. analysed the IQE of the AlGaN MQWs on AlGaN with various dislocation densities [39]. Under weak excitation with an excess carrier density of $1 \times 10^{18} \text{ cm}^{-3}$, the IQE was >70% when the dislocation density was $<10^8 \text{ cm}^{-2}$. When the dislocation density was $>10^8 \text{ cm}^{-2}$, the IQE decreased rapidly and approached zero at 10^{10} cm^{-2} . Therefore, reducing the dislocation density and improving the crystal quality are the keys to improving the device IQE. With the small lattice mismatch between AlN and high Al-content AlGaN, AlN single-crystal substrates with low dislocation densities should be ideal for the fabrication of AlGaN UV LEDs. However, the growth of high-quality, large, and low-cost AlN single crystals remains challenging. As an effective alternative, the epitaxially laterally overgrown (ELO) AlN template on a sapphire substrate is often used to demonstrate AlGaN LEDs with a threading dislocation density as low as $\sim 10^8 \text{ cm}^{-2}$ [40,41]. In particular, the dislocation density of ELO AlN templates grown by Kim et al. on the patterned sapphire substrates was as low as $5 \times 10^7 \text{ cm}^{-2}$. The maximum EQE of 266-nm and 278-nm LEDs fabricated on these temples were 1.9% and 3.3%, respectively [42]. Moreover, Susilo et al. used a simple and inexpensive method to prepare AlN template on sapphire substrate; the technique was physical vapour deposition followed by a face-to-face annealing in a nitrogen atmosphere at 1700 °C [43]. The threading dislocation density of these AlN films (thicknesses = 350 nm) was similar to that of ELO AlN films. Through experimental comparison, they found that the EQE of the AlGaN LED fabricated on these AlN templates (0.75% at 20 mA) was comparable to that fabricated on an ELO AlN/sapphire substrate (0.78%). Lattice mismatch between AlN and sapphire substrates was a key factor affecting the crystal quality of AlN grown on sapphire. In response to this problem, Chen et al. introduced graphene between a sapphire substrate and an AlN template, and the screw dislocation density and edge dislocation density of AlN decreased from 1.06×10^9 and $6.29 \times 10^9 \text{ cm}^{-2}$ to 2.67×10^8 and $2.45 \times 10^9 \text{ cm}^{-2}$, respectively [44]. From experimental comparison, the light output power of the device with graphene was much greater than that without graphene under the same injection current.

MQWs are the active regions of LED devices, which would directly determine the quantum efficiency of the device. Kaneda et al. fabricated a series of LED devices with novel uneven AlGaN MQWs on a (0001) sapphire with a 1° miscut relative to the *m*-plane [45]. This type of MQW reduced dislocation density and enhanced carrier localisation. Using this uneven MQW, the IQE of the device was as high as 60% at 298 nm. In addition, Sun et al. fabricated LEDs using wavy AlGaN MQWs on sapphire substrates with a large misorientation angle (4°) [46]. According to the photoluminescence spectrum, the IQE of the peak emission at 276 nm could reach 93%. Numerical simulations revealed that this structure could help to confine the carriers in MQW and improve IQE.

To achieve a high IQE, in addition to preparing the high performance MQWs, high injection efficiencies of electrons and holes in the MQWs are extremely important. Because of the large differences in electron and hole mobilities in AlGaN, the injected electrons may pass through the MQWs without recombination, leading to a low IQE. Thus, EBL is commonly used to confine more electrons and holes in the active region and to subsequently improve the QE of AlGaN UV LEDs. To improve the ability of EBL to block electrons and holes, many types of EBLs have been designed [47–52]. Zhang et al. used a *p*-AlGaN superlattice as EBL instead of the traditional single-layer *p*-AlGaN [51]. The EQE of AlGaN LED using *p*-AlGaN superlattice EBL increased by 90% compared with that of the device using single-layer EBL, and the efficiency droop was suppressed. In addition, they also used graded *p*-type AlGaN as EBL, which could generate a polarisation-induced electric field that can enhance the hole injection, and the EQE of the peak emission at 275 nm of the fabricated LED based on this structure EBL was 7.6% [52].

Excitingly, Takano et al. reported a DUV LED with an EQE of 20% at 275 nm, which is the highest EQE of DUV LEDs reported so far

[53]. They used a patterned sapphire substrate to reduce the dislocation density of AlN, Rh with a high reflectivity (68%) at 275 nm as the electrode of p-type layer, and finally, a resin with high transmittance at 275 nm to package the LED to further improve the LEE (as shown in Fig. 3(e) and (f)).

Fig. 4 summarises the EQE of typical AlGaN-based LEDs reported. The EQE of most DUV LEDs is <10% and much <1% when the wavelength is < 250 nm because of the challenge of p-type doping of high Al-content AlGaN and the low LEE of DUV LEDs. Therefore, despite the extensive research, the performance of DUV LEDs remains low, and related theoretical and experimental research should be further strengthened.

3.1.1.3. Design and fabrication of AlGaN UV LD. Compared with LEDs, LDs have better monochromaticity, greater intensity, higher directivity, and better temporal and spatial coherence. Therefore, AlGaN-based LDs have great potential in various fields such as high-density data storage, material processing, DUV lithography, DUV laser Raman spectroscopy, and optical communication. Limited by the low p-type doping efficiency of AlGaN with high Al contents, the development of AlGaN UV LDs with emission wavelengths in the UVC range faces great challenges. In 2008, Yoshida et al. demonstrated an ultraviolet 336 nm AlGaN MQWs laser diode, and 336 nm was long the shortest wavelength for room-temperature electrically pumped AlGaN-based LDs until 2018 [76]. Zhang et al. shortened the shortest laser wavelength record of AlGaN-based LDs to 271.8 nm at room temperature [77]. They realised electrically pumped AlGaN LDs with a p-type AlGaN cladding layer by using distributed polarisation doping on a high-quality single-crystal AlN substrate. A low operation voltage of 13.8 V at a lasing threshold current of 0.4 A can be observed as shown in Fig. 5(a). The hexagonal pyramid-shaped hillocks on the surface of p-side cladding, which originate from the threading dislocations of the AlN single-crystal substrate, considerably influenced the emergence of the laser. The laser could only be excited when the p-electrode did not overlap with the hillocks (as shown in Fig. 5(b)). Sato et al. reported a room-temperature operated AlGaN UVB LD at 298 nm [78]. The device was realised on a sapphire by using a lattice-relaxed, thick $\text{Al}_{0.6}\text{Ga}_{0.4}\text{N}$ underlying layer and a composition-graded p-AlGaN cladding layer. With the increase in the width of the p-electrode, the threshold current density decreased obviously.

3.1.1.2. AlGaN UV photodetectors. UV photodetectors have important applications in many important fields. In particular, as discussed in section 1, UVC photodetectors, commonly called as solar-blind photodetectors, are not interfered by background noise from solar radiations on the surface of the earth. Therefore, they have high signal-to-noise ratios, which have important applications in many civil and military fields, such as flame detection, missile early warning, and space exploration.

In the past two decades, AlGaN-based photoresistors (sometimes called photoconductors), p-(i)-n homo/heterojunction photodiodes, Schottky photodiodes, metal–semiconductor–metal (MSM) photodetectors, and phototransistors have been reported, and many important results have been achieved [79–90]. Among them, p-(i)-n junction photodiodes have the advantages of low noise and rapid response, and p-(i)-n junction is regarded as one of the most promising device structure. After years of development, AlGaN-based solar-blind ultraviolet detectors have made rapid progress. Similar to AlGaN-based LEDs and LDs, to improve the performance of high Al-content AlGaN UV detectors, the related research mainly focuses the improvement of the quality of the p-type layer and optimisation of the device structure. Kalra et al. introduced an AlN/AlGaN superlattice buffer to obtain a high-quality absorbing AlGaN epi-layer and used a graded p-AlGaN layer to improve the p-contact [91]. The zero-bias EQE of the device at 289 nm was 92%, and the detectivity could reach 6.1×10^{14} Jones. Subsequently, Chen et al. introduced a graded n-AlGaN layer between the n-AlGaN layer and i-AlGaN layer [92]. They thought that the graded n-AlGaN layer could improve photogenerated carriers' separation, transmission, and collection. The measured EQE of the device at 274 nm was 78.1% at zero-bias and 92.6% at 5 V reverse bias. Recently, AlGaN avalanche photodiodes based on p-i-n junctions have attracted increasing attention in recent years [93–98]. Their high avalanche multiplication gain enables them to detect ultraweak signals, which has important application prospects in scientific and technological fields such as cosmic background detection or quantum information. Owing to the continuous breakthrough of AlN single-crystal substrate growth technology, the development of high Al-content AlGaN-based avalanche photodiodes has accelerated in recent years. Reddy et al.

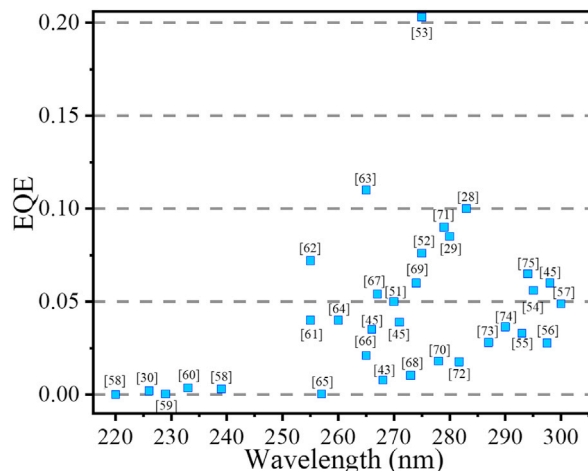


Fig. 4. EQE of typical AlGaN-based LEDs reported so far [28–30, 43, 45, 51–75].

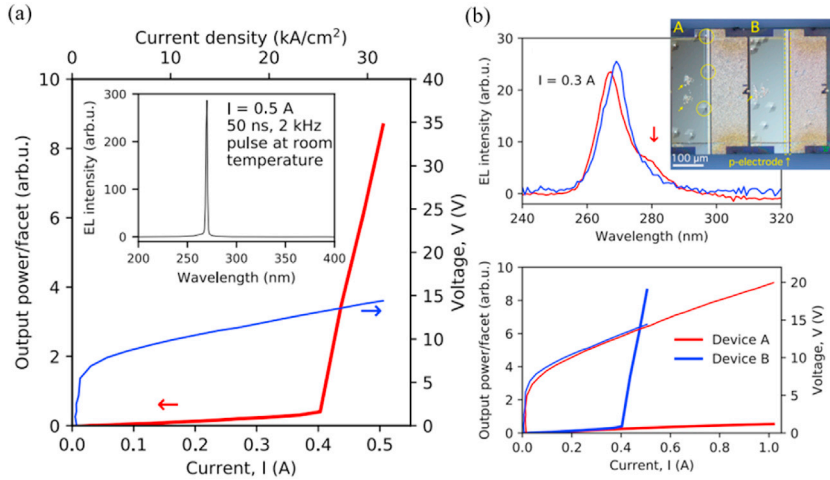


Fig. 5. (a) Current–voltage and the emission power characteristic curves of an AlGaN-based LD. The inset figure shows the edge emission spectrum at a forward current of 0.5 A. (b) Performance comparison between the two devices with and without p-electrode stepping on the hexagonal pyramid-shaped hillocks. When the p-electrode overlaps with the hillocks (yellow circle in device A), a shoulder appears on the edge of the emission peak and a laser cannot be generated [77]. Copyright (2019) The Japan Society of Applied Physics.

realised an AlGaN avalanche photodiode with high gain and large area using an AlN single-crystal substrate as shown in Fig. 6(a) [93]. The area of the device was approximately $25000 \mu\text{m}^2$. When the reverse bias voltage was $>340 \text{ V}$, the gain of the device could reach 10^5 under 255 nm UV illumination with a power density $<1 \mu\text{W cm}^{-2}$ (Fig. 6(b)). The high gain in this device was attributed to a high breakdown field of $\sim 9 \text{ MV cm}^{-1}$ as a consequence of low threading and screw dislocation densities of $<10^3 \text{ cm}^{-2}$. However, because the AlN substrates generally have absorption in the UVC region, a normal incidence detector structure is designed [99–101]. At the same time, to achieve good Ohmic contact, a p-GaN thin layer was inserted between the upper electrode and p-AlGaN. The p-GaN thin layer with a narrow bandgap absorbs the incident UV light, thus reducing the IQE of the device. Therefore, the growth of transparent AlN single crystals with high deep-UV transparency and the fabrication of high-quality p-AlGaN Ohmic contact must be further investigated to improve the performance of Al-rich AlGaN-based photodetectors.

In addition to junction photodiode, planar MSM photodetectors have attracted attention due to their simple structure, easy fabrication and integration, and low capacitance per unit area. The typical structure of MSM photodetectors can be regarded as a combination of two back-to-back Schottky junctions. The existence of two Schottky barriers in a MSM photodetector could effectively block the

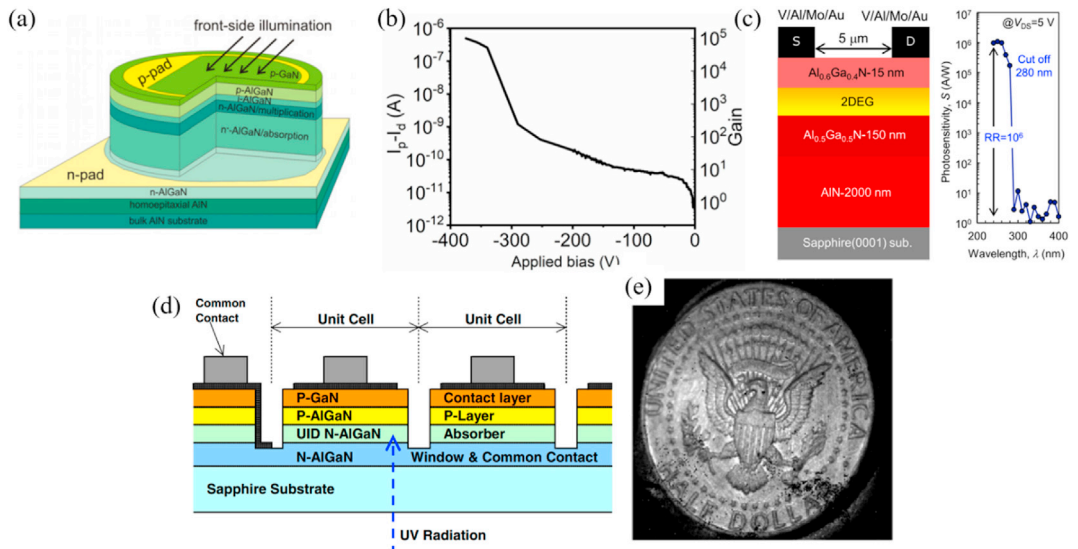


Fig. 6. (a) Structure of the AlGaN avalanche photodiode. (b) Difference between the dark current and photocurrent and the gain as a function of applied bias of AlGaN avalanche photodiodes [93]. Reprinted from Ref. [93], with the permission of AIP Publishing. (c) Structure and response spectrum of the AlGaN MSM photodetector [106]. Reprinted from Ref. [106], with the permission of AIP Publishing. (d) Cross section of the back-illuminated AlGaN p-i-n photodiode array. (e) UV reflection image taken with the 256 × 256 AlGaN FPA [109].

current flow, resulting in a highly low dark current of the device. For a long period of time in the past, relevant research focused on improving the performance of AlGaN MSM UV photodetectors by improving the crystalline quality of materials and increasing the metal-semiconductor contact barrier [79,102–104]. Recently, considering that planar MSM photodetectors have good adaptability to AlGaN two-dimensional electron gas (2DEG) with high electron mobility, an effective gain improvement of the device is expected to be realised [105,106]. Yoshikawa et al. fabricated a series of $\text{Al}_{0.6}\text{Ga}_{0.4}\text{N}/\text{Al}_{0.5}\text{Ga}_{0.5}\text{N}$ 2DEG MSM UV detectors and investigated the effects of electrode materials and rapid annealing conditions on the photoelectric characteristics of the device [106]. The optimised $\text{Al}_{0.6}\text{Ga}_{0.4}\text{N}/\text{Al}_{0.5}\text{Ga}_{0.5}\text{N}$ MSM UV photodetector has a responsivity of 10^6 A/W under 250 nm illumination at 5 V bias as shown in Fig. 6(c). The response rejection ratio ($R_{250 \text{ nm}}/R_{400 \text{ nm}}$) was approximately 10^6 . However, due to the persistent photoconductivity (PPC) effect caused by the trap effect of AlGaN heterojunction interface defects, the device had a considerably long fall time ($>1000 \text{ s}$).

With the development of GaN technology and integrated optoelectronic technology, solar-blind imaging devices with AlGaN-based focal plane arrays (FPAs) have been successfully realised [107,108]. In 2001, Lamarre et al. demonstrated a 256×256 AlGaN solar-blind UV-FPA with $30 \times 30 \mu\text{m}$ unit cells ($256 \times 256/30$) (Fig. 6(d)), and a UV reflection image of a U.S. half-dollar coin (3.0 cm diameter) was taken by this device as shown in Fig. 6(e) [109]. After that, the research progress of AlGaN-based FPAs for solar-blind UV and extreme UV (EUV) photodetection slowed down [110–112]. Although the maximum resolution of AlGaN solar-blind FPAs was improved to $640 \times 512/15$ by Robert et al. [111], the device quantum efficiency remained $<80\%$.

In summary, considerable progresses have been made in the research on AlGaN-based optoelectronic devices in recent years. However, AlGaN-based optoelectronic devices still face many great challenges. The EQE of AlGaN-based LEDs (especially those with emission wavelength $<250 \text{ nm}$) needs to be further improved. The performance of AlGaN-based UVC LDs is highly poor. In addition, to realise weak-signal detection, it is urgent to develop AlGaN-based photodetectors and FPAs with high sensitivity, high quantum efficiency, and high gain. To achieve a breakthrough in AlGaN-based optoelectronic devices, high-quality epitaxial growth and high-efficiency p-type doping of Al-rich AlGaN are the keys and also the focus of future research.

3.1.2. AlGaN-based microelectronic devices

3.1.2.1. AlGaN high-power devices. Because the E_b of semiconductor materials is positively related to the bandgap, Al-rich AlGaN with ultra-wide bandgap should have a large E_b and therefore have wide application prospects in the field of high-power devices. Because p-type doping of Al-rich AlGaN is still a challenge, recent research on Al-rich AlGaN-based two-terminal power devices has mainly focused on Schottky diodes, and great progress has been made [113–117]. Zhang et al. reported an $\text{Al}_{0.85}\text{Ga}_{0.15}\text{N}$ lateral Schottky barrier diode with specific on-resistance and breakdown voltage of $5 \Omega \text{ cm}^2$ and 2 kV, respectively [113]. Moreover, the on/off ratio of the device is as high as 10^6 . In addition, Fu et al. realised an AlN-based Schottky barrier diode with breakdown voltage $>1 \text{ kV}$ [114]. The on/off ratio of the device is approximately 10^5 .

Compared with two-terminal devices, the structure of three-terminal devices is more complex; however, they are useful and have a wide range of applications. High-electron-mobility transistors (HEMTs) based on AlGaN/GaN heterostructures have been partially industrialised. However, these HEMTs take GaN as the channel and do not really make use of the electrical properties of the UWBG AlGaN materials [118–120]. In recent years, with progress of research on the 2DEG of AlGaN heterojunction, AlGaN-based HEMTs have

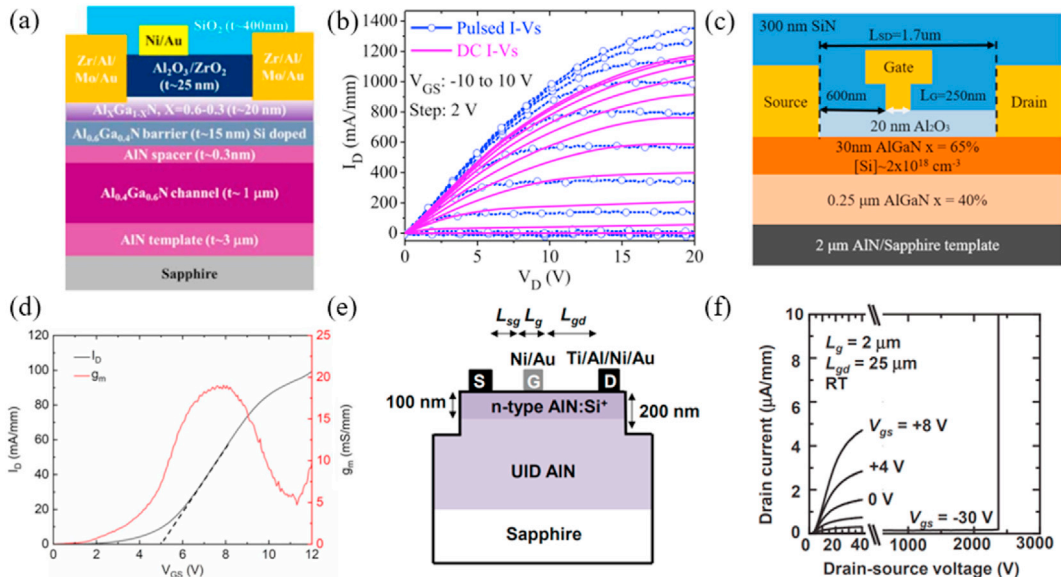


Fig. 7. (a) Structure and (b) output characteristic of the AlGaN-based MOS-HEMT [124]. Copyright (2020) The Japan Society of Applied Physics. (c) Schematic of the structure and (d) transfer characteristic of the E-mode AlGaN-based MOS-HEMT [127]. (e) Schematic of the structure and (f) output characteristic of the AlN-based MESFET [129]. Copyright (2018) The Japan Society of Applied Physics.

attracted increasing attention. To obtain good Ohmic contact for source and drain, Zr has been used as electrode material for source and drain of AlGaN-based HEMTs [121]. Meanwhile, to reduce the gate leakage current, Hu et al. fabricated AlGaN-based metal-oxide-semiconductor (MOS)-HEMTs for the first time with SiO₂ as the gate insulator [122]. When the gate voltage (V_{GS}) was 6 V, the drain saturation current density of the device reached 600 mA/mm. Xue et al. used the microchannel structure to improve the current density of AlGaN-based HEMTs [123]. By introducing a microchannel structure, the drain saturation current density of the device increased from 480 mA/mm to 910 mA/mm at a gate voltage of 2 V. More recently, Gaevski et al. achieved a significant increase in current density current density by further optimising the device structure (Fig. 7(a)) [124]. The reverse graded AlGaN was used as a barrier layer to ensure better Ohmic contact for the source and the drain. When the gate voltage was 12 V, the drain saturation current density of the device was as high as 1.17 A/mm (Fig. 7(b)). In addition, the breakdown voltage of the device was close to 1 kV with a gate to drain the spacing of 8 μ m.

As discussed in section 2.2.1, for high-power devices, E-mode devices are much safer than their D-mode counterparts in practical applications. Klein et al. demonstrated an E-mode AlGaN-based HEMT, with a threshold voltage of 0.5 V, by using a combination of gate recess etching and fluorine ions [125]. By using *p*-AlGaN as the gate, Douglas et al. reported E-mode AlGaN HEMTs with a maximum threshold voltage of 0.3 V [126]. Xue et al. fabricated normally off AlGaN-based MOS-HEMTs with high threshold voltage via fluorine treatment (Fig. 7(c)) [127]. A threshold voltage of 5 V and a maximum drain current density of 105 mA/mm at $V_{GS} = 12$ V can be clearly observed as shown in Fig. 7(d). The current on/off ratio was as high as 10^{10} .

In addition to AlGaN-based HEMTs, AlGaN-based metal-semiconductor field-effect transistors (MESFETs) have also been reported in recent years. Muhtadi et al. fabricated an Al_{0.65}Ga_{0.35}N-based MESFET on a high-quality AlN template (defect density = $\sim 1 \times 10^8$ – 2×10^8 cm⁻²) [128]. When the gate voltage was 2 V, the drain saturation current density of the device was approximately 100 mA/mm at room temperature. When the operating temperature increased to 200 °C, the drain saturation current density of the device changed by approximately 5%. Okumura et al. reported Si-doped *n*-AlN channel MESFETs (Fig. 7(e)) [129]. At room temperature, the breakdown voltage of the device with a gate to drain the spacing of 25 μ m reached 2370 V as shown in Fig. 7(f). However, due to the high activation energy of the Si donor, the drain saturation current density was only 8.7 μ A/mm at a gate voltage of 8 V.

3.1.2.2. AlGaN RF/microwave devices. With the proposal and development of fifth generation mobile communication technology, GaN-based RF/microwave devices have gained popularity all over the world owing to their excellent high-frequency characteristics. Similar to high-power devices, although AlGaN/GaN heterostructures have been widely used in GaN-based RF/microwave devices, the research on AlGaN-based RF/microwave devices is still quite preliminary. In recent years, research on Al-rich AlGaN RF/microwave devices has emerged. The RF performance of an MESFET with Al_{0.7}Ga_{0.3}N doping concentration of approximately 7×10^{18} cm⁻³ as the channel layer was measured in 2018 [130]. The f_T and f_{max} of the MESFET are 8.8 GHz and 24 GHz, respectively. AlGaN-based HEMTs can be used not only as high-power devices but also in the RF/microwave fields due to their high electron mobilities. Xue et al. reported an Al_{0.75}Ga_{0.25}N/Al_{0.6}Ga_{0.4}N RF/microwave HEMT [131]. The f_T and f_{max} of the device were 40 GHz and 58 GHz respectively, and the output power density was approximately 1.8 W/mm at 10 GHz. Further, in 2020, they explored the RF performance of the Al_{0.65}Ga_{0.35}N/Al_{0.4}Ga_{0.6}N microchannel HEMT [123]. The f_T and f_{max} of the device were 20 GHz and 36 GHz respectively, and its output power reached 2.7 W/mm at an operating frequency of 10 GHz.

With the development of materials and processes, Al-rich AlGaN-based microelectronic devices have developed rapidly in recent years. AlGaN-based two- and three-terminal power devices with breakdown voltage > 2 kV have been realised. The drain saturation current density of AlGaN-based HEMT exceeds 1 A/mm. In addition, although there are few relevant reports on AlGaN RF/microwave devices, the devices with f_T and f_{max} of > 10 GHz remain encouraging. Al-rich AlGaN-based microelectronic devices have important and broad application prospects, but they are in the nascent stages of development.

3.2. Diamond

Diamond is a UWBG semiconductor (the bandgap is approximately 5.47 eV), which has high electron and hole mobility (7300 cm²/V s for electron and 5300 cm²/V s for hole), high breakdown field (10 MV/cm), and high thermal conductivity (2290–3450 W/m K) [17],

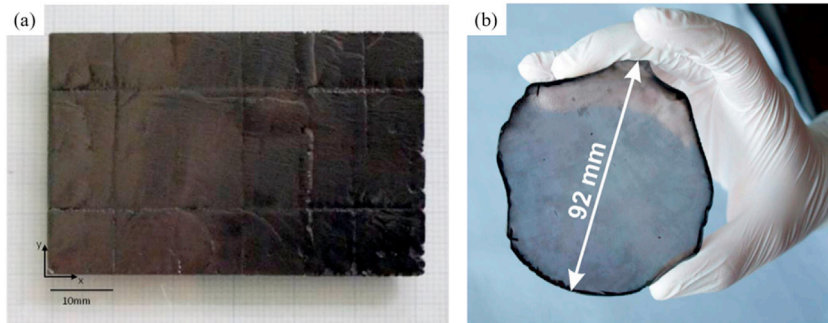


Fig. 8. (a) 2-inch diamond wafer grown by CVD [137]. Reprinted from Ref. [137], with the permission of AIP Publishing. (b) Freestanding unpolished diamond single crystal synthesised by heteroepitaxy on Ir/yttria stabilised zirconia (YSZ)/Si (0001) [138].

[132]. Therefore, diamond has considerable advantages in optoelectronic and microelectronic applications. However, the fabrication of low-cost, large-size, and high-quality diamond single-crystal wafers is challenging. The large surface energy makes it difficult to epitaxially grow high-quality diamond single-crystal films on a foreign substrate [133,134]. In addition, another challenge to making diamond-based devices is doping due to its rigid crystalline structure. The commonly used Boron acceptor impurities and Phosphorus donor impurities have high activation energies (0.38 eV and 0.43 eV, respectively) in a diamond material [135,136]. In recent years, significant efforts have been made to overcome these challenges. Yamada et al. successfully prepared a 2 inch diamond mosaic wafer (Fig. 8(a)) by using a repeated ‘tiled-clones’ method [137]. Schreck et al. obtained a freestanding diamond wafer with a diameter of approximately 92 mm (Fig. 8(b)) from an Ir substrate via ion bombardment [138]. On the other hand, high-concentration doping can form an impurity band in the band of diamond, thus reducing the activation energy of impurities [139,140]. P-type diamonds with high conductivity have been realised using this method. Although diamond n-type doping presents challenges, some studies have been performed, and the highest phosphorus doping concentration reported is $> 10^{20} \text{ cm}^{-3}$ [141–143]. The development of diamond-based devices is inseparable from the advancement of these growth and doping technologies. In this subsection, the research progress on diamond-based optoelectronic and microelectronic devices in recent years is mainly presented.

3.2.1. Diamond-based optoelectronic devices

Limited by the nature of the indirect bandgap and the n-type doping problem, the development of diamond-based LEDs and LDs is challenging. Currently, UV detectors have become the centre of diamond-based optoelectronic device research. Till now, diamond-based photoresistors [144,145], homo/heterojunction photodiodes [146–148], Schottky photodiodes [149–151], and MSM photodetectors [152–163] have been reported, and many significant results have been achieved.

P-(i)-n homojunction is considered one of the most ideal photodetector structures due to its rapid response, low noise, and high QE. Liu et al. fabricated a single-crystal diamond homogeneous p-i-n photodiode [147]. Under 5 V reverse bias, the peak responsivity of the device at 210 nm was approximately 1.69 A/W, and the UV-visible rejection ratio reached 2.17×10^3 . However, due to many defects in the n-type diamond, the response speed of the device was slow. To overcome the difficulty of n-type doping, some diamond UV photodetectors based on p-n heterojunction, Schottky junction, and MSM structure have been reported [148–157,159,160]. Typically, Lin et al. demonstrated an all-carbon diamond-based photoresistor [144]. First, high-quality diamond film was epitaxially grown on the diamond single-crystal substrate using chemical vapour deposition (CVD). Then, a pair of graphite electrodes was directly drawn on the diamond single-crystal film using laser-induced graphitisation of diamond (as shown in Fig. 9(a)). Under 50 V bias, the peak responsivity and detectivity at 218 nm of the device were 21.8 A/W and 1.39×10^{12} Jones, respectively. The device showed a high UV-visible rejection ratio ($R_{218 \text{ nm}}/R_{400 \text{ nm}}$) of 8.9×10^3 , as shown in Fig. 9(b)) and a fast response speed with rise/fall time of 310 $\mu\text{s}/330 \mu\text{s}$.

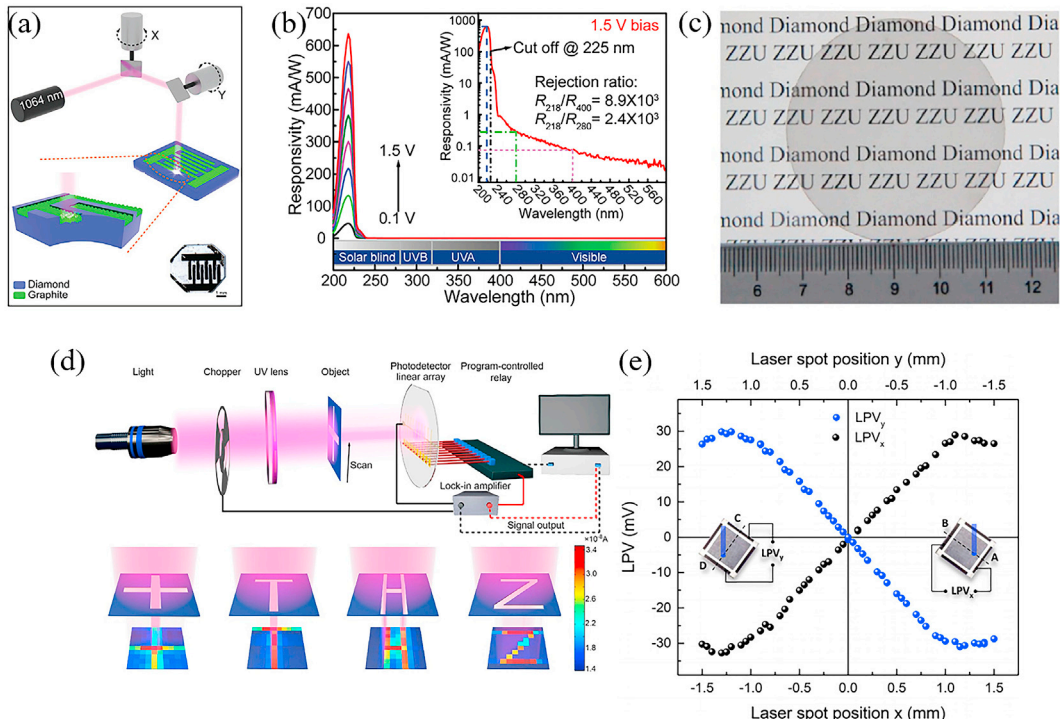


Fig. 9. (a) Schematic illustration and (b) response spectra of all-carbon diamond-based photoresistors [144]. (c) Optical image of the freestanding polycrystalline diamond film. (d) Schematic of the imaging system based on the polycrystalline diamond photodetector linear array [157]. Reprinted from Ref. [157], Copyright (2021), with permission from Elsevier. (e) Dependence of the lateral photovoltage amplitudes of the diamond-based position-sensitive detector on the position of the laser spot [151]. Reprinted from Ref. [151], with the permission of AIP Publishing.

Electric field across the photodetector is a key factor in the separation and collection of photogenerated carriers and has an important influence on the performance of photodetectors. For photodetectors with planar structures, Liu et al. fabricated a diamond-based photoresistor with a groove-shaped electrode structure [145]. The numerical simulation suggested that this groove-shaped electrode structure can improve the electric field intensity of the photosensitive region. Under the same test conditions, the peak responsivity of the device with groove electrodes increased by approximately 37% compared with that of the planar structure device.

Moreover, because the photoelectric characteristics of the surface have an important impact on the performance of the MSM photodetector, surface processing methods such as metal plasmons or surface pattern processing are used to improve the performance of diamond-based MSM photodetectors [155,156,159,160]. Chang et al. enhanced the UV absorption of the MSM photodetector by assembling of Pd nanoparticles on the diamond film [155]. The responsivity of the device was three orders higher than that of the device without Pd nanoparticles. In addition, Zhang et al. fabricated an MSM photodetector array with a vertical structure on a freestanding polycrystalline diamond film [157]. The freestanding polycrystalline diamond film (diameter = 2 inch) has highly visible transparency (Fig. 9(c)). At a bias voltage of 50 V and 228 nm, the responsivity and detectivity of the MSM photodetector cell are 45 mA/W and 2.92×10^{10} Jones, respectively. The UV-visible rejection ratio ($R_{228\text{ nm}}/R_{400\text{ nm}}$) of the cell is 46, the rise and fall times are <20 μs and 1.09 ms, respectively. Solar-blind images are obtained by using the diamond-based MSM photodetector array, as shown in Fig. 9(d). Additionally, a diamond-based position-sensitive detector using the photovoltaic effect of Schottky junction (Fig. 9(e)) was demonstrated by Prestopino et al. [151]. When the device was irradiated with UV light, the photogenerated electrons and holes drifted to the upper electrode and p-diamond, respectively, by the built-in electric field formed in the Schottky junction. In p-diamond, the hole concentration gradient is formed between the illuminated and non-illuminated regions, resulting in the so-called lateral photovoltaic effect, thus realise the resolution of the UV light spot position.

There has been considerable progress in the field of diamond-based photodetectors. However, the fabrication of high-performance diamond-based photodetectors faces some challenges. The high-quality epitaxial growth and high-efficiency n-type doping of diamond films are the main problems that must be resolved urgently.

3.2.2. Diamond-based microelectronic devices

3.2.2.1. Diamond high-power devices. As introduced at the beginning of section 3.2, the excellent electrical and thermal properties of diamond are prominent even in UWBG semiconductors. Therefore, diamond has good application prospects in the field of high-power devices. Till now, diamond-based two-terminal power devices, both p-(i)-n diodes and Schottky diodes, have shown the maximum reported breakdown voltages exceeding 10 kV [164,165]. Due to the great challenge of efficient n-type doping, more research has been focused on diamond-based Schottky diodes. In 2014, diamond-based Schottky diodes based on zirconium and ITO contacts was reported with a PFOM of as high as 244 MW/cm² at room temperature [24]. Generally, the conventional Schottky diode has a trade-off relationship between the specific on-resistance and the blocking voltage. To overcome this problem, a Schottky-p-n diode structure has been proposed, which constitutes a fully depleted n-type layer sandwiched by highly doped p-type layer and Schottky electrode [166,167]. By increasing the acceptor concentration in the p-type layer and the width of the n-type layer, the on-resistance can be reduced and the blocking voltage can be increased, respectively. Consequently, a diamond-based diode with a highly low specific on-resistance (0.03 m Ω cm²) and a blocking voltage of 55 V were achieved in diamond Schottky-p-n diode [166].

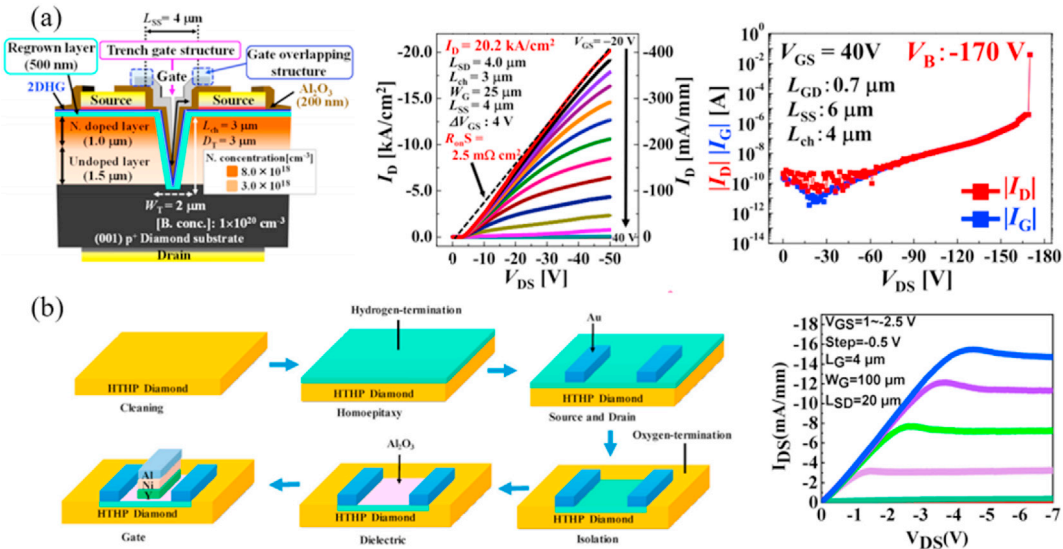


Fig. 10. (a) Schematic of the structure, output, and breakdown characteristics of the normally on H-terminal diamond-based MOSFET with a vertical structure [147]. © [2021] IEEE. Reprinted, with permission, from Ref. [147]. (b) Fabrication process and output characteristics of the normally off H-terminal diamond MOSFET using the Y/Ni/Al gate electrode [179]. Reprinted from Ref. [179], Copyright (2021), with permission from Elsevier.

In addition to the two-terminal devices, diamond-based three-terminal power devices, such as bipolar junction transistors (BJTs), junction field-effect transistor (JFETs), metal-oxide-semiconductor field-effect transistor (MOSFETs), and MESFETs have been realised and deeply investigated [168–183].

In 1989, Landstrass et al. found that the surface conductivity of diamonds (whether single-crystal or polycrystalline diamond) can be increased significantly by the hydrogen plasma treatment [184]. Subsequent studies revealed that H-plasma treatment leads to the formation of C–H bonds on the surface of diamonds, and two-dimensional hole gas (2DHG) forms, which improves the conductivity of the diamond surface [185]. Although the formation mechanism of H-terminated diamond surface 2DHG is still unclear, it has been widely used in diamond-based FETs because of its simple preparation process and the resulting excellent electrical properties. The performance of H-terminated diamond-based devices can be further improved by additional surface treatment. Using NO_2 adsorption treatment and Al_2O_3 passivation technique, Kasu's group have demonstrated a H-terminal diamond MOSFET with a high drain saturation current density of -1.35 A/mm at gate voltage of -5 V [172]. They further presented the highest reported breakdown voltage of -2608 V in a NO_2 p-type doped diamond MOSFETs with a 100-nm-thick Al_2O_3 passivation overlayer [173]. The PFOM was experimentally determined to be 344.6 MW/cm^2 , and a maximum drain current density of -288 mA/mm can be observed. In addition to the lateral structure, the vertical structures of H-terminated diamond MOSFETs have also been studied. Tsunoda et al. fabricated a vertical H-terminal diamond MOSFET with a trench gate structure (Fig. 10(a)) [174]. The device showed a very low specific on-resistance of approximately $2.5 \text{ m}\Omega \text{ cm}^2$, but the breakdown voltage was only -170 V (Fig. 10(a)).

In addition to the normally on devices, normally off H-terminal diamond MOSFETs have made significant progress. Kitabayashi et al. realised normally off MOSFETs by partially oxidising the surface of H-terminal diamond [175]. The distance between the gate and the drain (L_{gd}) was $24 \mu\text{m}$. When the gate voltage was -30 V , the drain saturation current density of the device was approximately -5.2 mA/mm . Moreover, the breakdown voltage of the device was as high as -2021 V . Alternatively, some low work function materials such as lanthanum boride (LaB_6), Al, Ti, and Y have been used as the gates to realise the normally off H-terminal diamond MOSFETs [176–179]. As shown in Fig. 10 (b), the normally off H-terminated diamond MOSFET with 5 nm Al_2O_3 dielectric layer and Y/Ni/Al gate electrode has been successfully fabricated [179]. The threshold voltage of the device was approximately -0.21 V . When the gate voltage was -2.5 V , the drain saturation current density of the device reached -16.14 mA/mm (Fig. 10(b)).

3.2.2.2. Diamond RF/microwave devices. Diamond is one of the first UWBG semiconductors as the channel of RF/microwave devices. The first diamond RF/microwave device was reported by Umezawa et al. in 2001 [186]. The f_T and f_{\max} were approximately 2.2 GHz and 7 GHz, respectively. Ueda et al. reported a polycrystalline diamond RF/Microwave FET with f_{\max} up to 120 GHz [187]. They thought that the polycrystalline diamond grain size ($\sim 100 \mu\text{m}$) is similar to the FET size, which makes the FET work on a diamond grain with a nearly single-crystal structure, thus leading to the high f_{\max} . Yu et al. used low-temperature atomic layer deposition technology to grow an Al_2O_3 insulating layer between the gate and the channel, and a RF/microwave device with an f_T of up to 70 GHz was fabricated [188]. Moreover, the maximum output power densities of diamond-based RF/microwave devices reported up to now have reached 3.8 W/mm at 1 GHz, 1 W/mm at 2 GHz, and 650 mW/mm at 10 GHz [189–191].

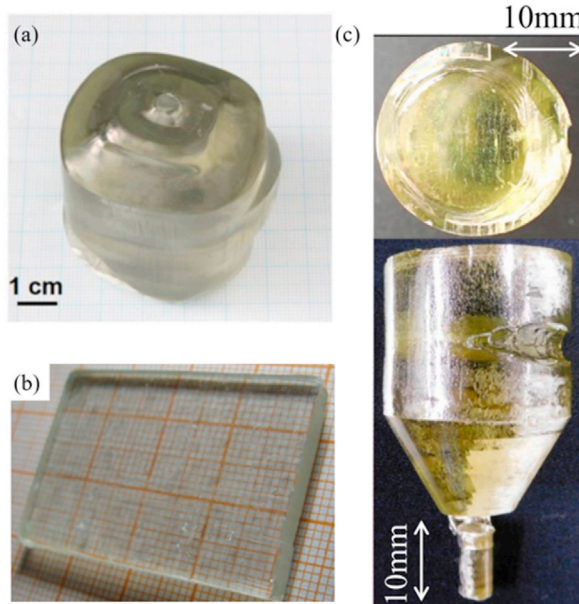


Fig. 11. Ga_2O_3 single-crystals grown by (a) Czochralski method [194], © The Electrochemical Society, reproduced by permission of IOP Publishing Ltd. All rights reserved, (b) EFG method [196], reprinted from Ref. [196], Copyright (2017), with permission from Elsevier, and (c) Bridgman method [195]. Reprinted from Ref. [195], Copyright (2021), with permission from Elsevier.

Many important achievements have been made in the research on diamond-based microelectronic devices, and diamond has shown considerable advantages in the field of microelectronics. However, more in-depth research is required. First, the formation mechanism of 2DHG in H-terminal diamond remains to be explored. The understanding of the formation mechanism could help further improve the electrical properties of H-terminal diamond. Second, for diamond-based high-power devices, the performance of normally off devices is far from that of normally on devices. As discussed in section 2.2.1, diamond-based normally off devices are considered highly suitable for power devices, whose the performance must be further improved. Finally, like optoelectronic devices, low-cost, high-quality, and large-size diamond single-crystal growth technology is crucial for improving the performance of diamond-based microelectronic devices and realise industrialisation.

3.3. Gallium oxide (Ga_2O_3)

Ga_2O_3 is an emerging UWBG semiconductor with various crystal structures, including α - Ga_2O_3 , β - Ga_2O_3 , γ - Ga_2O_3 , δ - Ga_2O_3 , and ϵ - Ga_2O_3 . Among them, β - Ga_2O_3 with a monoclinic structure is the most stable phase with a bandgap of approximately 4.6–5.0 eV [20, 192, 193]. Large-size and high-quality bulk Ga_2O_3 crystals have been prepared using the Czochralski method, the edge-defined film-fed growth (EFG) method, and the Bridgman method (Fig. 11) [194–196]. Due to the great success of Ga_2O_3 single-crystal growth and its excellent properties, there has been extensive research on Ga_2O_3 -based optoelectronic and microelectronic devices in recent years, and related developments are presented in detail in this subsection.

3.3.1. Ga_2O_3 -based optoelectronic devices

Owing to the suitable band gap and the excellent optoelectric properties, Ga_2O_3 is one of the most promising UWBG semiconductors for the application of solar-blind UV photodetection. High-performance Ga_2O_3 -based photodetectors with various device structures have been reported [146, 197–219]. Ga_2O_3 -based photoresistors have a simple structure, but the relative slow response speed hinders their practical applications [197, 220]. The slow response speed is generally considered to result from defects in Ga_2O_3 films [197, 210, 215]. Therefore, it is expected to shorten the response time by improving the crystal quality of Ga_2O_3 . Chen et al. fabricated a lateral UV photoresistor using a high-quality β - Ga_2O_3 single-crystal [198]. The rise and fall times of the device were <1 ms. Moreover, they used another single-crystal β - Ga_2O_3 as a filter to improve the spectral selectivity of the photoresistor (the response bandwidth: ~ 10 nm).

Similar to other UWBG semiconductors, Ga_2O_3 -based p-(i)-n homojunction devices are slow to develop due to their p-type doping problems [21, 192]. Although the p-type Ga_2O_3 has been demonstrated by Mg doping or GaN oxidation, the doping concentration, ionisation rate, and stability do not meet the requirement [199, 200]. Thus, constructing heterojunctions with other materials such as ZnO, GaN, diamond, p-Si, and Nb:SrTiO₃, has become a common method for realising high-performance Ga_2O_3 -based heterojunction photodiodes [146, 201–204]. Chen et al. grew a layer of α - Ga_2O_3 thin film on a ZnO single-crystal substrate via molecular beam epitaxy (MBE) to form a Ga_2O_3 -based heterojunction photodiode with a vertical structure [201]. The avalanche gain began to appear when the reverse bias voltage was >30 V. Under 40 V reverse bias, the peak response of the device at 254 nm was as high as 1.1×10^4 A/W. The theoretical simulation indicated that the maximum electric field intensity around the electrode on the Ga_2O_3 side exceeded 2 MV/cm.

In addition to heterojunction photodiodes, Ga_2O_3 -based Schottky junction photodiodes have been reported [205, 221–224]. Li et al.

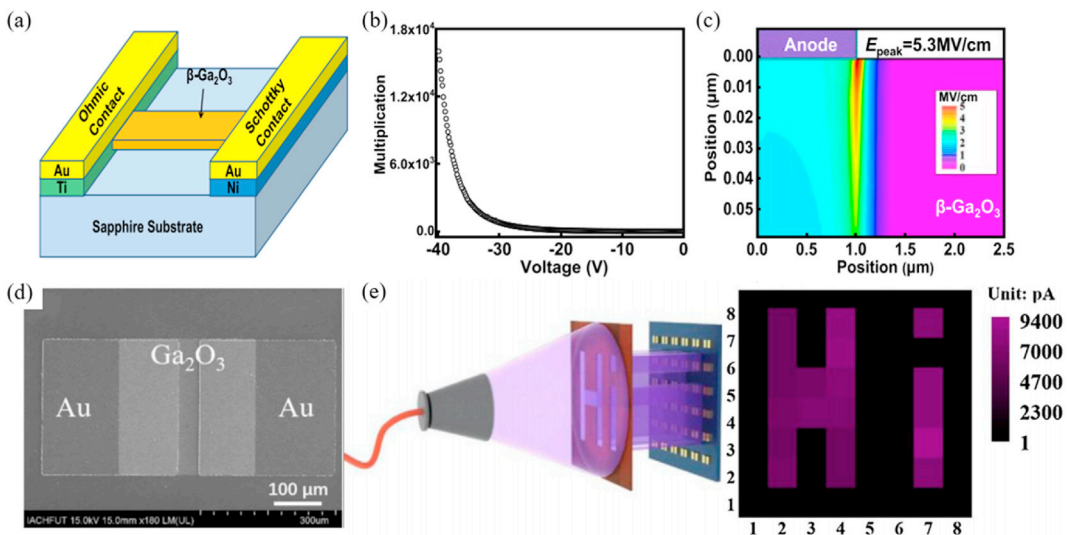


Fig. 12. (a) Schematic structure, (b) relationship between multiplication and reverse bias and (c) simulated electric field distribution of the Ga_2O_3 -based Schottky barrier avalanche photodiode [205]. © [2020] IEEE. Reprinted, with permission, from Ref. [205]. (d) Scanning electron microscopy image of the Ga_2O_3 -based MSM photodetector imaging array unit. (e) Schematic illustration of the setup for solar blind imaging and 2D current contrast map taken with Ga_2O_3 -based MSM photodetector imaging array [214]. Reprinted from Ref. [214], Copyright (2021), with permission from Elsevier.

explored the gain mechanism in the Schottky photodiode based on the Ga_2O_3 single-crystal flake exfoliated from Ga_2O_3 bulk single crystals as shown in Fig. 12(a) and (b) [205]. Under -40 V bias, the responsivity and normalised detectivity of the device were as high as 1.2×10^5 A/W and 2×10^{16} Jones, respectively, and the falling time was approximately 90 ms. The electric field intensity near the Schottky junction was calculated to be as high as 5.3 MV/cm under -40 V bias (Fig. 12(c)). Therefore, the high responsivity and high detectivity of this Schottky photodiode has been attributed to the carrier avalanche multiplication in the high electric field of the junction.

Ga_2O_3 -based MSM photodetectors have attracted considerable attention because of the simple fabrication process, low noise, and fast response [21, 225]. In recent years, Ga_2O_3 with various crystalline phases and even amorphous Ga_2O_3 have been used to fabricate Ga_2O_3 -based MSM photodetectors [206–210, 226, 227]. Zhou et al. reported the MSM solar-blind photodetectors based on amorphous Ga_2O_3 film with and without oxygen annealing [210]. The 90%–10% decay time and the rejection ratio of amorphous Ga_2O_3 photodetector annealed at 500 °C were approximately 150 ns and 2.74×10^5 , respectively. There has been extensive research on photodetector arrays based on Ga_2O_3 -based MSM photodetector units [211–214]. Chen et al. fabricated a 4×4 Ga_2O_3 MSM photodetector array [213]. At a bias voltage of 45 V, the peak responsivity and detectivity of the unit device at 256 nm were approximately 12.4 A/W and 1.9×10^{12} Jones, respectively, and the UV-visible rejection ratio ($R_{256 \text{ nm}}/R_{400 \text{ nm}}$) of the device was 4.6×10^4 . Xie et al. realised an 8×8 Ga_2O_3 MSM photodetector array by oxidising the Ga metal array and the structure of the MSM photodetector unit is shown in Fig. 12(d) [214]. Under 10 V bias, the responsivity of the unit device at 265 nm were approximately 0.72 A/W with rise/fall time of 1.1/0.03 s. Moreover, the excellent uniformity and repeatability of the performance of the device units enabled the photodetector array to be used as a DUV light image sensor (Fig. 12(e)).

The phototransistor is a three-terminal photodetector, and due to the presence of a gate electrode, it usually has higher photo-sensitivity than a two-terminal device. However, similar to the Ga_2O_3 -based photoresistors, some reported Ga_2O_3 -based phototransistors showed ultra-slow response speed due to the persistent photoconductivity (PPC) effect associated with the defects in the channel of the device [216, 217]. To avoid the PPC effect, Liu et al. fabricated a Ga_2O_3 -based phototransistor by using high-quality Ga_2O_3 single-crystal flake as the channel layer [218]. The time-dependent photocurrent ($I-t$) curve of the device under different drain voltages is shown in Fig. 13(a). When the gate voltage was -20 V and the drain voltage (V_{DS}) was 20 V, the responsivity and detectivity of the device were 4.79×10^5 A/W and 6.69×10^{14} Jones, respectively, and the fall time was <100 ms (Fig. 13(b)). Qin et al. fabricated a Ga_2O_3 -based phototransistor using high-quality Si-doped homoepitaxial single-crystal Ga_2O_3 thin film grown using MBE (Fig. 13(c)) [219]. To reduce the surface leakage current, they used SiO_2 to passivate the device. The photo-to-dark current ratio (I_{photo}/I_{dark}) was approximately 10^6 (Fig. 13(d)). When the gate voltage was -5 V and the drain voltage was 20 V, the peak responsivity of the device at 254 nm was 3×10^3 A/W with a fall time of <100 ms (Fig. 13(e)).

3.3.2. Ga_2O_3 -based microelectronic devices

3.3.2.1. Ga_2O_3 high-power devices. Benefiting from the progress of high-quality Ga_2O_3 growth technology, there has been increasing research on Ga_2O_3 -based high-power devices in recent years [228–254]. Due to the lack of high-quality and stable p-type Ga_2O_3 , the research on Ga_2O_3 -based two-terminal power devices has mainly focused on Schottky diodes and heterojunction diodes [228–230, 248],

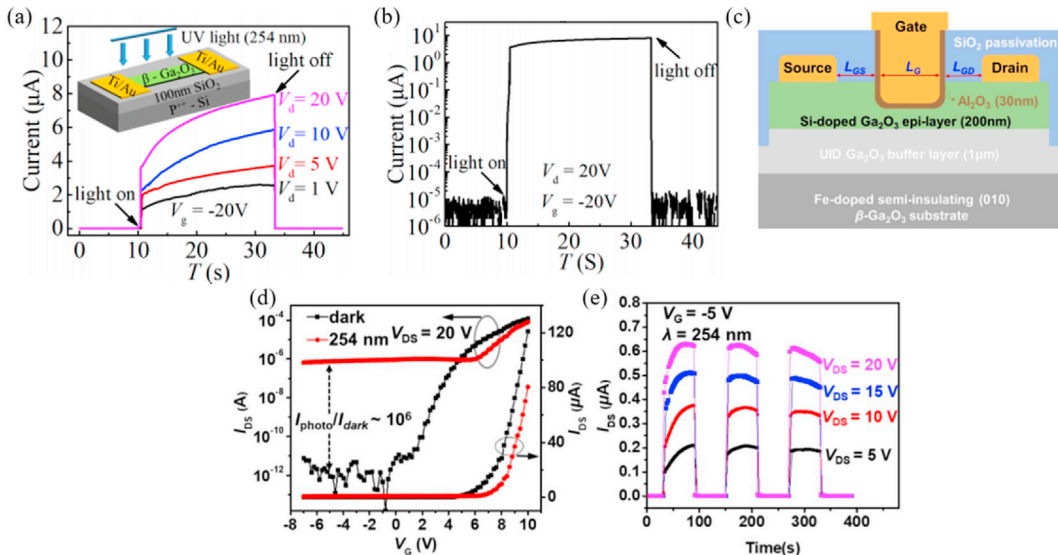


Fig. 13. (a) $I-t$ curves of the Ga_2O_3 -based phototransistor based on high-quality Ga_2O_3 single-crystal flakes at different drain voltages. (b) Log-scale $I-t$ curve of the device at the drain voltage of 20 V [218]. © [2018] IEEE. Reprinted, with permission, from Ref. [218]. (c) Schematic structure, (d) transfer, and (e) $I-t$ characteristics of the Ga_2O_3 -based phototransistor fabricated using MBE [219]. © [2019] IEEE. Reprinted, with permission, from Ref. [219].

250–254]. Hu et al. fabricated Schottky diodes with field-plated lateral structures using high-quality Ga_2O_3 single-crystal flakes [228]. When the distance between the anode and the cathode (L_{ac}) increased from 16 μm to 24 μm , the breakdown voltage of the device increased from 2.25 kV to >3 kV. However, the specific on-resistance of the device has also increased from 10.2 $\text{m}\Omega \text{ cm}^2$ to 24.3 $\text{m}\Omega \text{ cm}^2$. In addition, the device with L_{ac} of 16 μm had a large PFOM of 500 MW/cm^2 . Wang et al. demonstrated a $p\text{-NiO}_x/n\text{-Ga}_2\text{O}_3$ heterojunction diode with a breakdown voltage of 1.22 kV (Fig. 14(b)) [229]. Under 5 V forward bias, the specific on-resistance of the device was 1.08 $\text{m}\Omega \text{ cm}^2$, and the calculated PFOM was as high as 1.38 GW/cm^2 .

For three-terminal devices, Tetzner et al. realised high-performance Ga_2O_3 -based MOSFETs by using high-quality Si-doped $\beta\text{-Ga}_2\text{O}_3$ thin film homoepitaxy on a $\beta\text{-Ga}_2\text{O}_3$ single-crystal substrate [234]. Depending on the L_{gd} , the threshold voltage of the device varied from -25 to -14 V. When L_{gd} was 10 μm , the breakdown voltage of the device reached 1830 V, and the PFOM was 155 MW/cm^2 . To further improve the breakdown voltage of the device, in 2020, Lv et al. introduced a T-shape gate field-plated and source field-plated structures to D-model Ga_2O_3 -based MOSFETs to weaken the electric field crowding effect [235]. When L_{gd} was 4.8 μm , the threshold voltage, breakdown voltage, and PFOM of the device were -18 V, 1.4 kV, and 277 MW/cm^2 , respectively. When L_{gd} was 17.8 μm , the breakdown voltage of the device was as high as 2.9 kV. In addition, they also realised E-mode Ga_2O_3 -based MOSFETs through oxygen annealing [236]. When L_{gd} was 17 μm , the threshold voltage of the device was 4.1 V. After introducing double source-connected field plates, the breakdown voltage of the device could reach as high as >3 kV. However, the device had a high specific on-resistance, and thus the performance of the device needs further improvement. Fin FET is one of the most popular designs and has a fin-shaped channel surrounded by the gate terminal. Fin FET devices have better short channel control and are easier to manufacture than the traditional planar transistors [255]. Research on Ga_2O_3 -based fin FETs has been carried out [237,238,246]. Generally, when the fin width is sufficiently narrow, the depletion region formed by the gate is enough to pinch off the channel and realise the E-mode device. Hu et al. fabricated a normally off Ga_2O_3 fin FET with a fin width of 330 nm [237]. Its threshold voltage, specific on-resistance, and breakdown voltage were 1.2–2.2 V, 13–15 $\text{m}\Omega \text{ cm}^2$, and >1 kV, respectively. Li et al. demonstrated a significant enhancement of the channel mobility and an obvious reduction of specific on-resistance in Ga_2O_3 -based fin FETs through post-deposition annealing [238]. Moreover, they realised the normally off multi-fin transistors for the first time. A breakdown voltage of 2.66 kV and a specific on-resistance of 25.2 $\text{m}\Omega \text{ cm}^2$ can be observed, as shown in Fig. 14(a), and the calculated PFOM was as high as 280 MW/cm^2 .

Ga_2O_3 -based heterojunction field-effect transistors (HJFETs) have attracted increasing attention and achieved some remarkable results [229,232,239,244]. Wang et al. reported a high performance $p\text{-NiO}_x/n\text{-Ga}_2\text{O}_3$ HJFET as shown in Fig. 14(b) [229]. The adoption of bi-layer $p\text{-NiO}_x$ with low and high doping concentrations could enhance the channel depletion and improve the breakdown voltage of the device. The PFOM was as high as 390 MW/cm^2 . In addition, similar to AlGaN/GaN heterojunctions, an emerging UWBG semiconductor alloy (GaAl)₂O₃ was used to form heterojunctions with Ga_2O_3 to realise Ga_2O_3 -based HEMT [232,239,244]. Kalarickal et al. fabricated a $\beta\text{-}(\text{Al}_{0.18}\text{Ga}_{0.82})_2\text{O}_3/\text{Ga}_2\text{O}_3$ double-heterojunction FET, which exhibited a low specific on-resistance (Fig. 14(c)) [239]. Simultaneously, to improve the breakdown voltage, they overlapped the gate with an extreme- κ /low- κ composite dielectric to reduce the electric field crowding effect. When L_{gd} was 3.5 μm , the breakdown voltage and specific on-resistance of the device were 840 V and 1.72 $\text{m}\Omega \text{ cm}^2$, respectively, corresponding to a PFOM of 408 MW/cm^2 .

3.3.2.2. Ga_2O_3 RF/microwave devices. Compared with Ga_2O_3 -based power devices, the research on Ga_2O_3 -based RF/microwave devices started relatively late. The first Ga_2O_3 -based RF/microwave device was reported by Green et al. in 2017 [256]. They fabricated an RF/microwave MOSFET using n-type Ga_2O_3 with a doping concentration of approximately $1 \times 10^{18} \text{ cm}^{-3}$ as the channel layer. The f_T ,

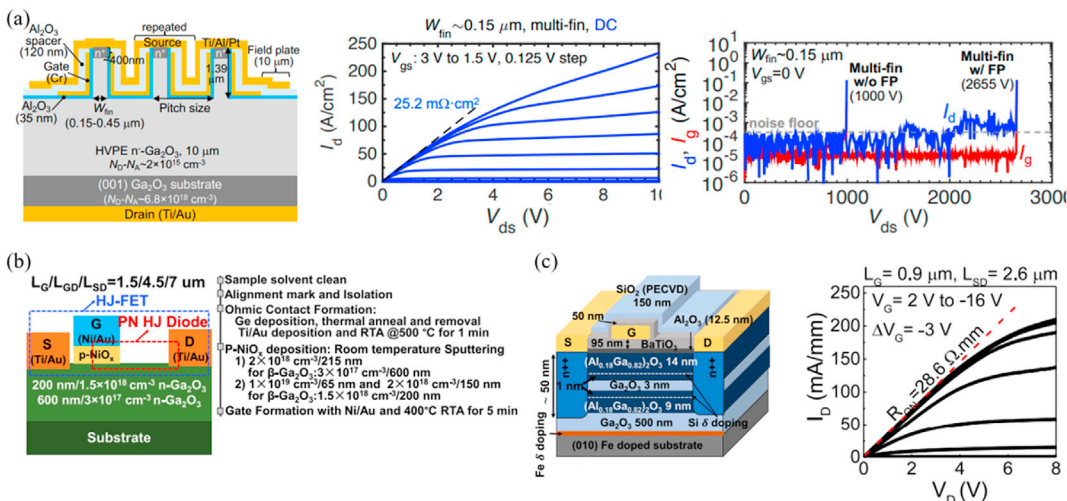


Fig. 14. (a) Schematic structure, output, and breakdown characteristics of E-mode vertical Ga_2O_3 -based multi-fin FETs [238]. © [2019] IEEE. Reprinted, with permission, from Ref. [238]. (b) Cross-sectional device schematic view of the $p\text{-NiO}_x/\text{Ga}_2\text{O}_3$ heterojunction diode and HJFET [229]. © [2021] IEEE. Reprinted, with permission, from Ref. [229]. (c) Schematic structure and output characteristics of the $(\text{AlGa})_2\text{O}_3/\text{Ga}_2\text{O}_3$ double-heterojunction FET [239]. © [2021] IEEE. Reprinted, with permission, from Ref. [239].

f_{\max} , and maximum output power density of the device were 3.3 GHz, 12.9 GHz, and 0.23 W/mm (at 800 MHz), respectively. Xia et al. fabricated a Ga_2O_3 RF/microwave FET through delta doping; f_T could reach 27 GHz [257]. Moser et al. reported a Ga_2O_3 -based MOSFET with an output power density of 715 mW/mm at 1 GHz (measured at pulsed condition) [258]. However, when the device was measured under continuous wave condition, its output power at 1 GHz was reduced to >200 mW/mm. Lv et al. explored the improvement of the RF/microwave characteristics of Ga_2O_3 -based MOSFETs via oxygen annealing [259]. They found that the current collapse effect of the device was suppressed to a certain extent after oxygen annealing, which was attributed to the neutralisation of impurities in the Ga_2O_3 buffer layer. The f_T and f_{\max} of the device after oxygen annealing were 1.8 GHz and 4.2 GHz, respectively. Under continuous wave test conditions, the maximum output power density of the device at 1 GHz operating frequency was as high as 400 mW/mm.

With advances in Ga_2O_3 single-crystal and epitaxial growth technology, Ga_2O_3 -based microelectronic devices have developed rapidly. Especially in recent years, high-performance Ga_2O_3 -based power devices have emerged continuously, and Ga_2O_3 -based RF/microwave devices have also attracted increasing attention. However, the performance of Ga_2O_3 -based microelectronic devices is far from reaching its theoretical limit. This means that Ga_2O_3 -based microelectronic devices still have great room for improvement.

3.4. Other UWBG semiconductors

In addition to the three UWBG semiconductors introduced in Section 3.1–3.3, some other UWBG semiconductors, such ZnGa_2O_4 , MgZnO and BN, have attracted significant attention due to their high application potential in the field of optoelectronics or/and microelectronics. This subsection briefly introduces the development of these representative materials and their related applications.

3.4.1. Zinc gallate (ZnGa_2O_4)

ZnGa_2O_4 is a type of UWBG semiconductor with a spinel structure and a bandgap of 4.6–5.25 eV [260]. For a long time, ZnGa_2O_4 has been well-known for its numerous applications in the field of photoluminescence and catalysis [261–265]. With the development of high-quality single crystal and epitaxial thin film preparation technology, ZnGa_2O_4 has exhibited considerable application prospects in the fields of optoelectronics and microelectronics due to its excellent material properties. Density functional theory (DFT) calculations have shown that there is considerable dispersion near the bottom of conduction band of ZnGa_2O_4 [266]. As is well known, electron effective mass (m_e^*) can be calculated using the following formula:

$$\frac{1}{m_e^*} = \frac{1}{\hbar} \frac{d^2 E}{dk^2} \quad (14)$$

where \hbar is the reduced Planck constant, E is the electron energy, and k is the wavevector of electron wave function. Therefore, the large dispersion indicates that the electron effective mass near the bottom of conduction band is small, which leads to a high electron mobility [267]. Galazka et al. achieved an electron mobility of as high as $100 \text{ cm}^2/\text{V s}$ in a ZnGa_2O_4 bulk crystal with an electron concentration of 10^{19} cm^{-3} [268]. Another interesting feature of ZnGa_2O_4 is its unique antisite defects. Ideally, the ZnGa_2O_4 crystal is a spinel structure

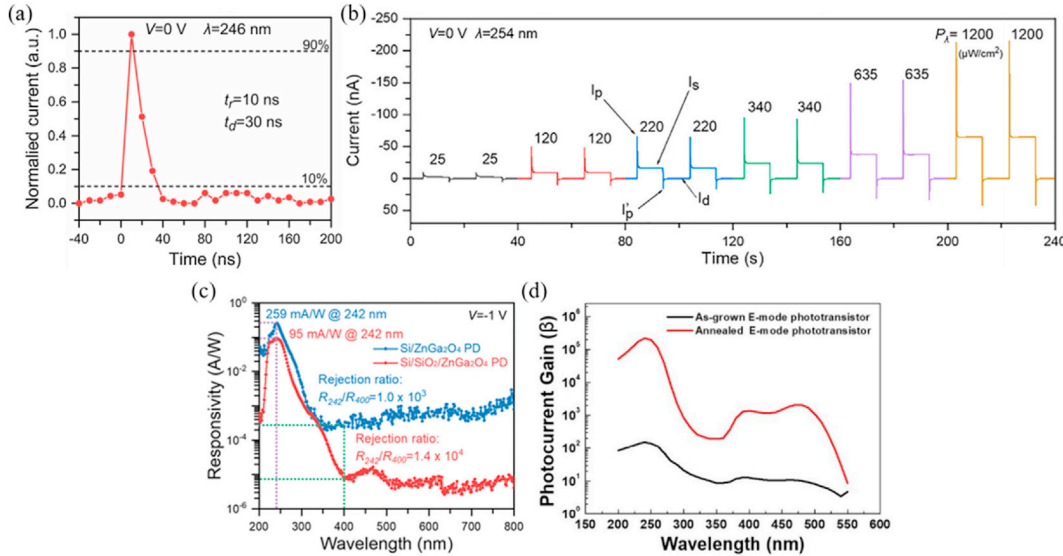


Fig. 15. (a) Transient photoresponse of the ZnGa_2O_4 MSM photodetectors with asymmetric electrodes at 0 V bias [272]. Reprinted from Ref. [272], Copyright (2020), with permission from Elsevier. (b) I - t characteristics of the p-Si/ ZnGa_2O_4 heterojunction photodiode under different light intensities at 0 V bias [273]. Reprinted from Ref. [273], with the permission of AIP Publishing. (c) Responsivity spectra of p-Si/ ZnGa_2O_4 and p-Si/ SiO_2 / ZnGa_2O_4 heterojunction photodiodes under -1 V bias [274]. (d) Photoconductive gain of as-grown and annealed E-mode ZnGa_2O_4 phototransistors [278]. Reprinted (adapted) with permission from Ref. [278]. Copyright 2020 American Chemical Society.

with Zn^{2+} at the centre of the tetrahedron and Ga^{3+} at the centre of the octahedron. However, due to the similar ionic radii of Zn^{2+} and Ga^{3+} as well as the micro imbalance of Zn and Ga in $ZnGa_2O_4$, the so-called antisite defects of Ga substituting Zn for tetrahedral centre (Ga_{Zn}) or Zn substituting Ga for octahedral centre (Zn_{Ga}) will be formed [269,270]. Ga_{Zn} is a donor defect, and Zn_{Ga} is an acceptor defect. In 2020, Chikoidze et al. demonstrated a p-type $ZnGa_2O_4$ film by introducing the acceptor antisites (Zn_{Ga}) [270]. The high-temperature Hall effect hole concentration was as high as $2 \times 10^{15} \text{ cm}^{-3}$, while hole mobilities were $\mu_h = 7\text{--}10 \text{ cm}^2/\text{V s}$ in the 680–850 K temperature range. Therefore, the antisite defects provide a new scheme for high-quality and stable $ZnGa_2O_4$ p-type doping and n-type doping, which is expected to overcome the doping challenges faced by almost all UWBG semiconductors.

Since 2018, UV photodetectors based on $ZnGa_2O_4$ thin films with different structures have been reported, and some surprising results have been obtained [271–278]. Tsai et al. prepared an MSM photodetector based on the MOCVD epitaxial $ZnGa_2O_4$ film [271]. The device has a high peak responsivity of 86.3 A/W at 230 nm. Additionally, a novel self-powered solar-blind photodetector was constructed by fabricating asymmetric pairs of Au Schottky electrodes on the $ZnGa_2O_4$ film. At 0 V bias, the peak responsivity at 246 nm was approximately 22.2 mA/W with an UV-vis rejection ratio of 1.3×10^4 . The device offered an ultra-fast response speed with the shortest-record rise/decay time of 10/30 ns (Fig. 15(a)). The heterojunction formed by $ZnGa_2O_4$ and Si has also been reported [273,274,279]. Han et al. demonstrated a self-powered solar-blind photodiode based on p-Si/ $ZnGa_2O_4$ heterojunction, and a transient peak

Table 2
Performance of UWBG semiconductor-based UV photodetectors.

Structure	Dark current (nA)	Responsivity (A/W)	Rise/fall time (ms)	Normalised detectivity (Jones)	Reference
AlGaN p-i-n junction	$<10^{-3}$ (-10 V)	0.211 (0 V@289 nm)	<13	6.1×10^{14}	[91]
AlGaN p-i-n junction	–	0.173 (0 V@274 nm)	–	–	[92]
		0.205 (-5 V@274 nm)			
AlGaN p-i-n junction	~ 10 (-10 V)	0.15 (0 V@271 nm)	6.5×10^{-6} /-	–	[300]
AlGaN avalanche photodiode	$<10^{-4}$ (-60 V)	~ 0.06 (-5 V@255 nm)	–	–	[93]
AlGaN avalanche photodiode	10^{-3} (-60 V)	0.036 (0 V@249 nm, backside illumination) 0.058 (0 V@246 nm, frontside illumination)	–	–	[94]
AlN heterojunction	–	0.067 (0 V@195 nm)	8×10^{-5} /0.4	–	[90]
AlGaN MSM	$\sim 10^{-2}$ (10 V)	10^6 (5 V@250 nm)	$200/ > 10^6$	–	[106]
Diamond photoresistor	$\sim 5 \times 10^3$ (50 V)	21.8 (50 V@218 nm)	0.31/0.33	1.39×10^{12}	[144]
diamond p-i-n junction	350 (-5 V)	1.69 (-5 V@210 nm)	–	–	[147]
Diamond/ β - Ga_2O_3 heterojunction	~ 4 (-15 V)	2×10^{-4} (0 V@244 nm)	–	6.9×10^9	[146]
Diamond Schottky junction	3.2×10^{-3} (3 V)	0.018 (3 V@220 nm)	120/560	–	[149]
Diamond Schottky junction	14.2×10^{-3} (-10 V)	3.71×10^{-3} (5 V@215 nm)	600/590	–	[150]
Diamond MSM	2×10^{-3} (20 V)	6.99×10^{-3} (20 V@240 nm)	115.5/157.1	–	[154]
Diamond MSM	$<10^{-3}$ (5 V)	0.057 (5 V@210 nm)	–	–	[155]
Diamond MSM	~ 10 (50 V)	0.045 (50 V@228 nm)	<0.02 /-	2.92×10^{10}	[157]
Diamond MSM	0.93 (60 V)	13 (60 V@222 nm)	1.3×10^{-3} / 0.203	–	[163]
β - Ga_2O_3 photoresistor	–	0.23 (5 V@262 nm)	0.48/0.38	–	[198]
β - Ga_2O_3 heterojunction	3.1 (-10 V)	43.31 (-10 V@254 nm)	–	–	[204]
α - Ga_2O_3/ZnO avalanche photodiode	–	1.1×10^4 (-40 V@254 nm)	–	–	[201]
β - Ga_2O_3 Schottky junction	–	10^{-3} (-1 V@248 nm)	<200	–	[223]
β - Ga_2O_3 Schottky avalanche photodiode	–	1.2×10^5 (-40 V@254 nm)	/90	2×10^{16}	[205]
ε - Ga_2O_3 MSM	23.5×10^{-3} (6 V)	230 (6 V@254 nm)	–	1.2×10^{15}	[208]
Amorphous Ga_2O_3 MSM	9.43×10^{-3} (10 V)	1.34 (10 V@250 nm)	$10^{-5}/1.5 \times$ 10^{-4}	–	[210]
β - Ga_2O_3 MSM avalanche photodiode	$<10^{-3}$ (20 V)	46 (20 V@254 nm)	/0.027	9.8×10^{15}	[207]
β - Ga_2O_3 transistor	5×10^{-3} ($V_{GS} = -20$ V, $V_{DS} = 20$ V)	4.79×10^5 ($V_{GS} = -20$ V, $V_{DS} = 20$ V @254 nm)	–	6.69×10^{14}	[218]
β - Ga_2O_3 transistor	$<10^{-3}$ ($V_{GS} = -5$ V, $V_{DS} = 20$ V)	3×10^3 ($V_{GS} = -20$ V, $V_{DS} = 20$ V @254 nm)	–	1.3×10^{16}	[219]
$ZnGa_2O_4$ heterojunction	<10 (-5 V)	7.5×10^{-3} (0 V@254 nm, stable responsivity) 0.041 (0 V@254 nm, transient responsivity)	<40	–	[273]
$ZnGa_2O_4$ heterojunction	5.7×10^{-3} (-1 V)	0.095 (-1 V@242 nm)	120/80	7.03×10^{12}	[274]
$ZnGa_2O_4$ MSM	–	0.022 (0 V@246 nm)	$10^{-5}/3 \times 10^{-5}$	–	[272]
$ZnGa_2O_4$ transistor	2×10^{-3} ($V_{GS} = 0$ V, $V_{DS} = 5$ V@240 nm)	474 ($V_{GS} = 0$ V, $V_{DS} = 5$ V@240 nm)	400/700	–	[278]
MgZnO Schottky junction	–	0.055 (0 V@265 nm)	0.02/0.3	–	[292]
MgZnO MSM	0.111 (10 V)	205 (10 V)	/280	–	[293]
MgZnO MSM	160 (25 V)	0.086 (25 V@235 nm)	–	–	[291]

current phenomenon could be observed when UV light was turned on and off at 0 V (Fig. 15(b)) [273]. The interface pyroelectric effect of the ZnGa₂O₄ film should be responsible for this transient spike photocurrent phenomenon, which could effectively enhance the responsivity and response speed of the device. Moreover, with the introduction of a thin SiO₂ insulation layer between ZnGa₂O₄ and p-Si, the UV-visible rejection ratio of the device increased by one order of magnitude under -1 V bias (Fig. 15(c)) [274]. Compared with the two-terminal devices, the phototransistor has excellent modulated light response performance. Horng's group demonstrated both E-mode and D-mode phototransistors based on the ZnGa₂O₄ film [278]. After annealing treatment, the E-model ZnGa₂O₄ phototransistor exhibited a large photocurrent gain of 2.21×10^5 at 240 nm (Fig. 15(d)). However, the UV-visible rejection and response speed must be further improved.

3.4.2. Magnesium zinc oxide ($MgZnO$)

$MgZnO$ is an attractive oxide semiconductor formed by alloying MgO with ZnO. Similar to AlGaN, by adjusting the ratio of Zn and Mg, the bandgap of $MgZnO$ can be adjusted from 3.3 eV (ZnO) to 7.8 eV (MgO). However, the epitaxial growth of $MgZnO$ films is more challenging than that of AlGaN due to the different crystalline structures of ZnO and MgO [280,281]. ZnO is usually stable in the form of wurtzite, while MgO has a rock salt structure. In the early days, most research focused on how to achieve high-quality hexagonal or cubic single crystal ZnMgO alloys with adjustable composition and bandgap in a wide range. UWBG ZnMgO alloys mostly have a cubic phase structure [282–284]. The photodetectors based on UWBG ZnMgO have been fabricated by using various methods [285–288]. However, the responsivity for the most reported devices is generally considerably low. In recent years, mixed-phase ZnMgO (m -ZnMgO) has attracted increasing attention in the field of UV photodetection because its internal grain boundary can effectively reduce the dark current and partially enhance the photocurrent [289–291]. Fan et al. fabricated a UWBG m -ZnMgO thin film with a single absorption edge, and its solar-blind photodetector exhibited a peak responsivity of 1.664 A/W at 260 nm and an UV/visible rejection of $>10^3$ under 10 V bias [290]. In addition, some related studies on the structural design and packaging of $MgZnO$ -based photodetectors have also been performed [292–294].

3.4.3. Boron nitride (BN)

BN is another novel type of UWBG semiconductor material, which has attracted considerable attention in recent years. BN has a variety of crystal structures, and among them hexagonal BN (h-BN) and cubic BN (c-BN) are most common [295–298]. Owing to its unique two-dimensional layered structure and excellent properties, h-BN has become one of the most popular research hotspots. Theoretical and experimental results showed that h-BN has a very high exciton binding energy (~250 meV for indirect exciton and ~700 meV for direct exciton); thus, it is expected to be used in the field of DUV lasers [297–299]. C-BN is an ideal material for high-power microelectronic devices in extreme environments due to its ultrahigh breakdown field (8–17.5 MV/cm), high thermal conductivity (940 W/m K for natural isotopic ratio and as high as 2145 W/m K for isotopically pure), high thermal stability, and high hardness [17,296]. At present, the research on BN is still in its nascent stages. Due to its excellent optical and electrical properties, BN-based optoelectronic and microelectronic devices can have broad development prospects.

4. Conclusions and prospects

In this paper, recent advances in optoelectronic and microelectronic devices based on UWBG semiconductors are briefly reviewed. Tables 2–4 present the performance parameters of some representative UWBG semiconductor-based optoelectronic and microelectronic devices. The research on UWBG semiconductors has grown explosively owing to their excellent optical and electrical properties. After more than 20 years of development, more novel characteristics of UWBG semiconductors and their great application potential in optoelectronic and microelectronic devices have been shown.

Considerable efforts have been made to obtain high-quality UWBG semiconductor materials and high-performance UWBG semiconductor-based devices, and great success has been achieved. However, it should be noted that there is still a long way to go to realise the large-scale industrialisation of UWBG semiconductor-based optoelectronic and microelectronic devices. Compared with traditional semiconductors, the research on UWBG semiconductor materials and devices is still underdeveloped. The development of UWBG semiconductor-based optoelectronic and microelectronic devices faces many challenges and opportunities, some of which are highlighted below:

(1) The growth of high-quality UWBG semiconductors

High-quality single-crystals are crucial for realising high-performance UWBG semiconductor-based optoelectronic and microelectronic devices. Whether they are used as substrates or as active layers in optoelectronic and microelectronic devices, the defects (including dislocations and point defects) in the UWBG semiconductor greatly affect the performance of devices. As mentioned in section 3, the progress of UWBG semiconductor single-crystal growth technology has greatly promoted the development of their optoelectronic and microelectronic devices. However, the growth of UWBG semiconductor bulk single crystals with low cost, high quality, and large size is still a challenge, especially for AlN and diamond. Moreover, epitaxial growth technology requires more in-depth research. It is not only an important basis for realising high-performance UWBG semiconductor-based devices, but also an important platform for studying the basic physical properties of UWBG semiconductors. In recent years, the rapid development of real-time in situ grown monitoring and computational physics has provided new opportunities for the epitaxial growth of high-quality UWBG semiconductor films. The combination of experimental real-time observation and theoretical numerical simulation can provide a more profound understanding of the growth kinetics of UWBG semiconductors. Therefore, it is believed that in the near future, there will be

Table 3

The DC characteristics of some representative UWBG semiconductor-based power devices.

Structure	Breakdown voltage (kV)	Specific on-resistance ($\Omega \text{ cm}^2$)	On/off ratio	Threshold voltage (V)	Maximum drain current density (mA/mm)	PFOM (MW/cm ²)	Reference
AlGaN Schottky junction	2	5	10^6	–	–	–	[113]
AlN Schottky junction	>1	–	10^5	–	–	–	[114]
AlGaN HEMT	–	–	5×10^7	–	600 ($V_{GS} = 6 \text{ V}$)	–	[122]
AlGaN HEMT	0.08	–	–	–	910 ($V_{GS} = 2 \text{ V}$)	–	[123]
AlGaN HEMT	~0.6	–	–	-11	1170 ($V_{GS} = 12 \text{ V}$)	–	[124]
AlGaN HEMT	–	–	–	0.5	35 ($V_{GS} = 6.6 \text{ V}$)	–	[125]
AlGaN HEMT	–	–	10^{10}	5	105 ($V_{GS} = 12 \text{ V}$)	–	[127]
AlGaN MESFET	–	–	–	-13.5	100 ($V_{GS} = 2 \text{ V}$)	–	[128]
AlN MESFET	0.51	–	100	–	8.7×10^{-3} ($V_{GS} = 8 \text{ V}$)	–	[129]
Diamond Schottky junction	1	–	–	–	–	244	[24]
Diamond Schottky-p-n diode	–	3×10^{-5}	10^{12}	–	–	–	[166]
H-terminal diamond MOSFET	–	–	–	11	-1350 ($V_{GS} = -5 \text{ V}$)	–	[172]
H-terminal diamond MOSFET	-2.608	19.74×10^{-3}	$>10^7$	6.9	-288 ($V_{GS} = -7 \text{ V}$)	345	[173]
H-terminal diamond MOSFET	-0.17	2.5×10^{-3}	10^7	20.5	-406 ($V_{GS} = -20 \text{ V}$)	–	[174]
H-terminal diamond MOSFET	-2.021	–	10^8	-3.9	-5.2 ($V_{GS} = -30 \text{ V}$)	–	[175]
H-terminal diamond MOSFET	–	–	10^7	-0.021	-16.14 ($V_{GS} = -2.5 \text{ V}$)	–	[179]
$\beta\text{-Ga}_2\text{O}_3$ heterojunction junction	1.22	1.08×10^{-3}	10^9	–	–	1380	[229]
$\beta\text{-Ga}_2\text{O}_3$ Schottky junction	2.25	10.2×10^{-3}	10^9	–	–	500	[228]
$\beta\text{-Ga}_2\text{O}_3$ MOSFET	1.83	–	10^9	-14	49 ($V_{GS} = 10 \text{ V}$)	155	[234]
$\beta\text{-Ga}_2\text{O}_3$ MOSFET	1.4	7.08×10^{-3}	10^9	-18	230 ($V_{GS} = 15 \text{ V}$)	277	[235]
$\beta\text{-Ga}_2\text{O}_3$ fin FET	>1	$13\text{--}18 \times 10^{-3}$	10^8	1.2–2.2	–	–	[237]
$\beta\text{-Ga}_2\text{O}_3$ fin FET	2.66	25.2×10^{-3}	10^8	1.8	–	280	[238]
$\beta\text{-Ga}_2\text{O}_3$ HJFET	1.115	3.19×10^{-3}	10^{10}	-13	330 ($V_{GS} = 0 \text{ V}$)	390	[229]
$\beta\text{-Ga}_2\text{O}_3$ /(GaAl) ₂ O ₃ HEMT	0.84	1.72×10^{-3}	–	–	–	408	[239]

Table 4

Summary of UWBG semiconductor-based RF/microwave devices.

Structure	Cut-off frequency (GHz)	Maximum oscillation frequency (GHz)	Output power density (W/mm)	Reference
AlGaN MESFET	8.8	24	–	[130]
AlGaN HEMT	40	58	1.8 (@10 GHz)	[131]
AlGaN HEMT	20	36	2.7 (@10 GHz)	[123]
Diamond MOSFET	70	80	–	[188]
Diamond MOSFET	31	31	3.8 (@1 GHz)	[189]
Diamond MOSFET	15	36	1.04 (@2 GHz)	[190]
Diamond MOSFET	18	34	0.65 (@10 GHz)	[191]
$\beta\text{-Ga}_2\text{O}_3$ MOSFET	3.3	12.9	0.23 (@800 MHz)	[256]
$\beta\text{-Ga}_2\text{O}_3$ MOSFET	–	–	0.2 (@1 GHz)	[258]
$\beta\text{-Ga}_2\text{O}_3$ MOSFET	1.8	4.2	0.4 (@1 GHz)	[259]
$\beta\text{-Ga}_2\text{O}_3$ MESFET	27	16	–	[257]

more breakthroughs in UWBG semiconductors epitaxial growth with advances in research.

(2) The realisation of high efficiency and stable doping

In general, the impurities doped into UWBG semiconductors often have high activation energies, which makes them difficult to ionise at room temperature. For example, Mg is a common acceptor impurity for p-type doping of AlGaN, and the activation energy of Mg acceptor increases with the increasing Al content. For AlN, the activation energy of Mg acceptor can reach as high as 0.51 eV [301]. The activation energies of donor impurity P and acceptor impurity B commonly used in diamond are 0.43 eV and 0.38 eV, respectively. Moreover, the strong self-compensation effect hinders the doping efficiency and stability of UWBG semiconductors. In general, the formation energy, $E_{form}(q)$, of a defect X in a charge state, q , can be expressed as [302,303]:

$$E_{form}(X, q) = E_{tot}(X, q) - E_{tot} - \sum_i n_i \mu_i + q(E_f + E_v) \quad (15)$$

where $E_{tot}(X, q)$ is the total energy of the supercell with a defect, X , and E_{tot} is the total energy for the equivalent perfect supercell of the semiconductor. n_i indicates the number of atoms i (impurity or host atoms) that are removed from ($n_i < 0$) or added into ($n_i > 0$) the supercell, μ_i is the corresponding chemical potential, E_f is the Fermi level with reference to the valence-band maximum E_v . If the acceptors are doped into the UWBG semiconductor, the Fermi level will decrease, the formation energy of the donor-like native point defects will decrease sharply, thereby compensating the acceptors. Some unintentional impurities introduced in the growth process may passivate the dopant and further reduce the ionisation efficiency of donor or acceptor impurities. Till now, there has been extensive research on doping, and many significant results have been achieved [136,141,304–306]. However, how to reduce the ionisation energy of impurities and suppress the self-compensation effect remains a key problem for future work.

(3) The design and optimisation of the devices

Structural upgrades and improvements are effective to improve the performance of semiconductor devices. Various structures, such as nanophotonics structure, 2DEG structure, and fin structure, have been introduced into the UWBG microelectronic and optoelectronic devices, and significant performance enhancement has been achieved. However, the QE of optoelectronic devices and the PFOM and maximum output power density of microelectronic devices have room for improvement. In the future, research on device design and manufacturing technology should be increased.

(4) The exploration of new UWBG materials

The emergence and development of new semiconductor materials can greatly promote the development of devices. In recent years, some emerging UWBG semiconductors, such as $ZnGa_2O_4$, $MgGa_2O_4$, $(GaAl)_2O_3$, BN, have attracted increasing attention due to their novel optical and electrical properties. The antisite defects in $ZnGa_2O_4$ and $MgGa_2O_4$ materials provide novel ideas for solving the doping problems of UWBG semiconductors. Therefore, the development of emerging materials will bring new opportunities for the research and application of UWBG semiconductor devices.

Acknowledgements

This work is supported by the National Natural Science Foundation of China (62074148, 61875194, 11727902, 12074372, 11974344, 61975204), the National Ten Thousand Talent Program for Young Top-notch Talents, the Key Research and Development Program of Changchun City (No. 21ZY05), 100 Talents Program of the Chinese Academy of Sciences and Youth Innovation Promotion Association, CAS (2020225).

References

- [1] T.H. Lee, The (pre-) history of the integrated circuit: a random walk, *IEEE Solid-State Cir Soc Newsletter* 12 (2) (2007) 16–22.
- [2] K. Shenai, The figure of merit of a semiconductor power electronics switch, *IEEE Trans. Electron. Dev.* 65 (10) (2018) 4216–4224.
- [3] Physical limitations on frequency and power parameters of transistors, in: E. Johnson (Ed.), 1958 IRE International Convention Record, 1965, pp. 27–34.
- [4] R.W. Keyes, Figure of merit for semiconductors for high-speed switches, *Proc. IEEE* 60 (2) (1972) 225.
- [5] B.J. Baliga, Fundamentals of Power Semiconductor Devices, Springer Science & Business Media, 2010.
- [6] S.M. Sze, Y. Li, K.K. Ng, Physics of Semiconductor Devices, John Wiley & Sons, 2021.
- [7] S.S. Lawrence, T. Suzue, T. Egawa, Breakdown enhancement of AlGaN/GaN HEMTs on 4-in silicon by improving the GaN quality on thick buffer layers, *IEEE Electron. Device Lett.* 30 (6) (2009) 587–589.
- [8] V.W.L. Chin, T.L. Tansley, T. Osotchan, Electron mobilities in gallium, indium, and aluminum nitrides, *J. Appl. Phys.* 75 (11) (1994) 7365–7372.
- [9] B.E. Foutz, S.K. O’Leary, M.S. Shur, L.F. Eastman, Transient electron transport in wurtzite GaN, InN, and AlN, *J. Appl. Phys.* 85 (11) (1999) 7727–7734.
- [10] Z. Guo, A. Verma, X. Wu, F. Sun, A. Hickman, T. Masui, et al., Anisotropic thermal conductivity in single crystal β -gallium oxide, *Appl. Phys. Lett.* 106 (11) (2015), 111909.
- [11] T.L. Chu, R.W. Kelm, The preparation and properties of aluminum nitride films, *J. Electrochem. Soc.* 122 (7) (1975) 995–1000.
- [12] Y. Taniyasu, M. Kasu, T. Makimoto, Increased electron mobility in n-type Si-doped AlN by reducing dislocation density, *Appl. Phys. Lett.* 89 (18) (2006), 182112.
- [13] G.A. Slack, R.A. Tanzilli, R.O. Pohl, J.W. Vandersande, The intrinsic thermal conductivity of AlN, *J. Phys. Chem. Solid.* 48 (7) (1987) 641–647.
- [14] T. Teraji, S. Koizumi, Y. Koide, T. Ito, Electric field breakdown of lateral Schottky diodes of diamond, *Jpn. J. Appl. Phys.* 46 (No. 9) (2007) L196–L198.
- [15] B.A. Fox, M.L. Hartsell, D.M. Malta, H.A. Wynands, C.T. Kao, L.S. Plano, et al., Diamond devices and electrical properties, *Diam. Relat. Mater.* 4 (5) (1995) 622–627.
- [16] M. Pomorski, E. Berdermann, A. Caragheorgheopol, M. Ciobanu, M. Kiš, A. Martemyanov, et al., Development of single-crystal CVD-diamond detectors for spectroscopy and timing, *Phys. Status Solidi* 203 (12) (2006) 3152–3160.
- [17] L. Lindsay, D.A. Broido, T.L. Reinecke, First-Principles determination of ultrahigh thermal conductivity of boron arsenide: a competitor for diamond? *Phys. Rev. Lett.* 111 (2) (2013), 025901.
- [18] K. Sasaki, A. Kuramata, T. Masui, E.G. Villora, K. Shimamura, S. Yamakoshi, Device-quality beta-Ga₂O₃ epitaxial films fabricated by ozone molecular beam epitaxy, *APPEX* 5 (3) (2012), 035502.
- [19] K. Ghosh, U. Singisetti, Ab initio velocity-field curves in monoclinic β -Ga₂O₃, *J. Appl. Phys.* 122 (3) (2017), 035702.
- [20] J.Y. Tsao, S. Chowdhury, M.A. Hollis, D. Jena, N.M. Johnson, K.A. Jones, et al., Ultrawide-bandgap semiconductors: research opportunities and challenges, *Adv. Electron. Mater.* 4 (1) (2018), 1600501.
- [21] C. Xie, X.T. Lu, X.W. Tong, Z.X. Zhang, Fx Liang, L. Liang, et al., Recent progress in solar-blind deep-ultraviolet photodetectors based on inorganic ultrawide bandgap semiconductors, *Adv. Funct. Mater.* 29 (9) (2019), 1806006.
- [22] R.C. Jones, Phenomenological description of the response and detecting ability of radiation detectors, *Proc IRE* 47 (9) (1959) 1495–1502.

- [23] A.I. Green, K.D. Chabak, E.R. Heller, R.C. Fitch, M. Baldini, A. Fiedler, et al., 3.8-MV/cm Breakdown Strength of MOVPE-Grown Sn-Doped beta-Ga2O3 MOSFETs, *IEEE Electron. Device Lett.* 37 (7) (2016) 902–905.
- [24] A. Traoré, P. Muret, A. Fiori, D. Eon, E. Gheeraert, J. Pernot, Zr/oxidized diamond interface for high power Schottky diodes, *Appl. Phys. Lett.* 104 (5) (2014), 052105.
- [25] M. Kneissl, T.Y. Seong, J. Han, H. Amano, The emergence and prospects of deep-ultraviolet light-emitting diode technologies, *Nat. Photonics* 13 (4) (2019) 233–244.
- [26] H.K. Cho, I. Ostermayr, U. Zeimer, J. Enslin, T. Wernicke, S. Einfeldt, et al., Highly reflective p-contacts made of Pd-Al on deep ultraviolet light-emitting diodes, *IEEE Photon. Technol. Lett.* 29 (24) (2017) 2222–2225.
- [27] M. Guttmann, A. Susilo, L. Sulmoni, N. Susilo, E. Ziffer, T. Wernicke, et al., Light extraction efficiency and internal quantum efficiency of fully UVC-transparent AlGaN based LEDs, *J. Phys. D Appl. Phys.* 54 (33) (2021), 335101.
- [28] Y. Kashima, N. Maeda, E. Matsuura, M. Jo, T. Iwai, T. Morita, et al., High external quantum efficiency (10%) AlGaN-based deep-ultraviolet light-emitting diodes achieved by using highly reflective photonic crystal on p-AlGaN contact layer, *APEX* 11 (1) (2017), 012101.
- [29] T.H. Lee, T.H. Park, H.W. Shin, N. Maeda, M. Jo, H. Hirayama, et al., Smart wide-bandgap omnidirectional reflector as an effective hole-injection electrode for deep-UV light-emitting diodes, *Adv. Opt. Mater.* 8 (2) (2020), 1901430.
- [30] D. Liu, S.J. Cho, J. Park, J. Gong, J.H. Seo, R. Dalmau, et al., 226 nm AlGaN/AlN UV LEDs using p-type Si for hole injection and UV reflection, *Appl. Phys. Lett.* 113 (1) (2018), 011111.
- [31] N. Maeda, M. Jo, H. Hirayama, Improving the light-extraction efficiency of AlGaN DUV-LEDs by using a superlattice hole spreading layer and an Al reflector, *Phys. Status Solidi* 215 (8) (2018), 1700436.
- [32] N. Maeda, J. Yun, M. Jo, H. Hirayama, Enhancing the light-extraction efficiency of AlGaN deep-ultraviolet light-emitting diodes using highly reflective Ni/Mg and Rh as p-type electrodes, *Jpn. J. Appl. Phys.* 57 (4S) (2018), 04FH8.
- [33] Y. Zhang, S. Krishnamoorthy, F. Akyol, J.M. Johnson, A.A. Allerman, M.W. Moseley, et al., Reflective metal/semiconductor tunnel junctions for hole injection in AlGaN UV LEDs, *Appl. Phys. Lett.* 111 (5) (2017), 051104.
- [34] S. Inoue, N. Tamari, M. Taniguchi, 150 mW deep-ultraviolet light-emitting diodes with large-area AlN nanophotonic light-extraction structure emitting at 265 nm, *Appl. Phys. Lett.* 110 (14) (2017), 141106.
- [35] M. Suzuki, T. Uenoyama, A. Yanase, First-principles calculations of effective-mass parameters of AlN and GaN, *Phys. Rev. B* 52 (11) (1995) 8132–8139.
- [36] S.H. Park, J.I. Shim, Carrier density dependence of polarization switching characteristics of light emission in deep-ultraviolet AlGaN/AlN quantum well structures, *Appl. Phys. Lett.* 102 (22) (2013), 221109.
- [37] S.M. Islam, K. Lee, J. Verma, V. Protasenko, S. Rouvimov, S. Bharadwaj, et al., MBE-grown 232–270 nm deep-UV LEDs using monolayer thin binary GaN/AlN quantum heterostructures, *Appl. Phys. Lett.* 110 (4) (2017), 041108.
- [38] C. Liu, Y.K. Ooi, S.M. Islam, H. Xing, D. Jena, J. Zhang, 234 nm and 246 nm AlN-Delta-GaN quantum well deep ultraviolet light-emitting diodes, *Appl. Phys. Lett.* 112 (1) (2018), 011101.
- [39] K. Ban, J. Yamamoto, K. Takeda, K. Ide, M. Iwaya, T. Takeuchi, et al., Internal quantum efficiency of whole-composition-range AlGaN multiquantum wells, *APEX* 4 (5) (2011), 052101.
- [40] H. Hirayama, S. Fujikawa, J. Norimatsu, T. Takano, K. Tsubaki, N. Kamata, Fabrication of a low threading dislocation density ELO-AlN template for application to deep-UV LEDs, *Phys. Status Solidi C* 6 (S2) (2009) S356–S359.
- [41] S. Kamiyama, M. Iwaya, S. Takanami, S. Terao, A. Miyazaki, H. Amano, et al., UV light-emitting diode fabricated on hetero-ELO-grown Al_{0.22}Ga_{0.78}N with low dislocation density, *Phys. Status Solidi* 192 (2) (2002) 296–300.
- [42] M. Kim, T. Fujita, S. Fukahori, T. Inazu, C. Pernot, Y. Nagasawa, et al., AlGaN-based deep ultraviolet light-emitting diodes fabricated on patterned sapphire substrates, *APEX* 4 (9) (2011), 092102.
- [43] N. Susilo, S. Hagedorn, D. Jaeger, H. Miyake, U. Zeimer, C. Reich, et al., AlGaN-based deep UV LEDs grown on sputtered and high temperature annealed AlN/sapphire, *Appl. Phys. Lett.* 112 (4) (2018), 041110.
- [44] Z. Chen, Z. Liu, T. Wei, S. Yang, Z. Dou, Y. Wang, et al., Improved epitaxy of AlN film for deep-ultraviolet light-emitting diodes enabled by graphene, *Adv. Mater.* 31 (23) (2019), 1807345.
- [45] M. Kaneda, C. Pernot, Y. Nagasawa, A. Hirano, M. Ippomatsu, Y. Honda, et al., Uneven AlGaN multiple quantum well for deep-ultraviolet LEDs grown on macrosteps and impact on electroluminescence spectral output, *Jpn. J. Appl. Phys.* 56 (6) (2017), 061002.
- [46] H. Sun, S. Mitra, R.C. Subedi, Y. Zhang, W. Guo, J. Ye, et al., Unambiguously enhanced ultraviolet luminescence of AlGaN wavy quantum well structures grown on large misoriented sapphire substrate, *Adv. Funct. Mater.* 29 (48) (2019), 1905445.
- [47] C. Chu, K. Tian, J. Che, H. Shao, J. Kou, Y. Zhang, et al., On the origin of enhanced hole injection for AlGaN-based deep ultraviolet light-emitting diodes with AlN insertion layer in p-electron blocking layer, *Opt Express* 27 (12) (2019) A620–A628.
- [48] C. Chu, K. Tian, M. Fang, Y. Zhang, L. Li, W. Bi, et al., On the Al_xGa_{1-x}-Al_yGa_{1-y}N/Al_xGa_{1-x}N (x > y) p-electron blocking layer to improve the hole injection for AlGaN based deep ultraviolet light-emitting diodes, *Superlattice. Microst.* 113 (2018) 472–477.
- [49] R.K. Mondal, V. Chatterjee, S. Pal, Effect of step-graded superlattice electron blocking layer on performance of AlGaN based deep-UV light emitting diodes, *Physica E Low Dimens. Syst. Nanostruct.* 108 (2019) 233–237.
- [50] M. Usman, M. Mansif, A.-R. Anwar, H. Jamal, S. Malik, N.U. Islam, Quantum efficiency enhancement by employing specially designed AlGaN electron blocking layer, *Superlattice. Microst.* 139 (2020), 106417.
- [51] Z.H. Zhang, C.S.W. Huang, C. Chu, K. Tian, M. Fang, Y. Zhang, et al., Nearly efficiency-droop-free AlGaN-based ultraviolet light-emitting diodes with a specifically designed superlattice p-type electron blocking layer for high Mg doping efficiency, *Nanoscale Res. Lett.* 13 (1) (2018) 122.
- [52] Z.H. Zhang, J. Kou, S.W.H. Chen, H. Shao, J. Che, C. Chu, et al., Increasing the hole energy by grading the alloy composition of the p-type electron blocking layer for very high-performance deep ultraviolet light-emitting diodes, *Photon. Res.* 7 (4) (2019) B1–B6.
- [53] T. Takano, T. Mino, J. Sakai, N. Noguchi, K. Tsubaki, H. Hirayama, Deep-ultraviolet light-emitting diodes with external quantum efficiency higher than 20% at 275 nm achieved by improving light-extraction efficiency, *APEX* 10 (3) (2017), 031002.
- [54] M. Ajmal Khan, E. Matsuura, Y. Kashima, H. Hirayama, Influence of undoped-AlGaN final barrier of MQWs on the performance of lateral-type UVB LEDs, *Phys. Status Solidi* 216 (18) (2019), 1900185.
- [55] M.A. Khan, T. Matsumoto, N. Maeda, N. Kamata, H. Hirayama, Improved external quantum efficiency of 293 nm AlGaN UVB LED grown on an AlN template, *Jpn. J. Appl. Phys.* 58 (SA) (2018), SAAF01.
- [56] R. Ni, C.C. Chuo, K. Yang, Y. Ai, L. Zhang, Z. Cheng, et al., AlGaN-based ultraviolet light-emitting diode on high-temperature annealed sputtered AlN template, *J. Alloys Compd.* 794 (2019) 8–12.
- [57] R. Ni, Z. Yu, Z. Liu, L. Zhang, L. Jia, Y. Zhang, Light extraction and auger recombination in AlGaN-based ultraviolet light-emitting diodes, *IEEE Photon. Technol. Lett.* 32 (16) (2020) 971–974.
- [58] M. Guttmann, F. Mehnke, B. Belde, F. Wolf, C. Reich, L. Sulmoni, et al., Optical light polarization and light extraction efficiency of AlGaN-based LEDs emitting between 264 and 220 nm, *Jpn. J. Appl. Phys.* 58 (SC) (2019), SCCB20.
- [59] D. Liu, S.J. Cho, J. Park, J.H. Seo, R. Dalmau, D. Zhao, et al., 229 nm UV LEDs on aluminum nitride single crystal substrates using p-type silicon for increased hole injection, *Appl. Phys. Lett.* 112 (8) (2018), 081101.
- [60] P.N. Lobo, F. Mehnke, L. Sulmoni, H.K. Cho, M. Guttmann, J. Glaab, et al., Milliwatt power 233 nm AlGaN-based deep UV-LEDs on sapphire substrates, *Appl. Phys. Lett.* 117 (11) (2020), 111102.
- [61] M. Ichikawa, T. Kemmochi, T. Mukai, M. Uomoto, T. Shimatsu, Fabrication of high power deep ultraviolet light-emitting diodes with glass lenses using atomic diffusion bonding, *ECS J. Solid State Sci. Technol.* 9 (1) (2019), 015004.
- [62] A. Pandey, J. Gim, R. Hovden, Z. Mi, An AlGaN tunnel junction light emitting diode operating at 255 nm, *Appl. Phys. Lett.* 117 (24) (2020), 241101.

- [63] A. Pandey, W.J. Shin, J. Gim, R. Hovden, Z. Mi, High-efficiency AlGaN/GaN/AlGaN tunnel junction ultraviolet light-emitting diodes, *Photon. Res.* 8 (3) (2020) 331–337.
- [64] P. Wang, A. Pandey, J. Gim, W.J. Shin, E.T. Reid, D.A. Laleyan, et al., Graphene-assisted molecular beam epitaxy of AlN for AlGaN deep-ultraviolet light-emitting diodes, *Appl. Phys. Lett.* 116 (17) (2020), 171905.
- [65] Y. Zhang, S. Krishnamoorthy, F. Akyol, S. Bajaj, A.A. Allerman, M.W. Moseley, et al., Tunnel-injected sub-260 nm ultraviolet light emitting diodes, *Appl. Phys. Lett.* 110 (20) (2017), 201102.
- [66] R. Ishii, A. Yoshikawa, K. Nagase, M. Funato, Y. Kawakami, Temperature-dependent electroluminescence study on 265-nm AlGaN-based deep-ultraviolet light-emitting diodes grown on AlN substrates, *AIP Adv.* 10 (12) (2020), 125014.
- [67] W. Shin, A. Pandey, X. Liu, Y. Sun, Z. Mi, Photonic crystal tunnel junction deep ultraviolet light emitting diodes with enhanced light extraction efficiency, *Opt Express* 27 (26) (2019) 38413–38420.
- [68] J. Lang, F.J. Xu, W.K. Ge, B.Y. Liu, N. Zhang, Y.H. Sun, et al., Greatly enhanced performance of AlGaN-based deep ultraviolet light emitting diodes by introducing a polarization modulated electron blocking layer, *Opt Express* 27 (20) (2019) A1458–A1466.
- [69] L. Zhang, Y. Guo, J. Yan, Q. Wu, Y. Lu, Z. Wu, et al., Deep ultraviolet light-emitting diodes based on a well-ordered AlGaN nanorod array, *Photon. Res.* 7 (9) (2019) B66–B72.
- [70] B.K. SaifAddin, A.S. Almogbel, C.J. Zollner, F. Wu, B. Bonef, M. Iza, et al., AlGaN deep-ultraviolet light-emitting diodes grown on SiC substrates, *ACS Photonics* 7 (3) (2020) 554–561.
- [71] N. Maeda, M. Jo, H. Hirayama, Improving the efficiency of AlGaN deep-UV LEDs by using highly reflective Ni/Al p-type electrodes, *Phys. Status Solidi* 215 (8) (2018), 1700435.
- [72] N. Zhang, F.J. Xu, J. Lang, L.B. Wang, J.M. Wang, Y.H. Sun, et al., Improved light extraction efficiency of AlGaN deep-ultraviolet light emitting diodes combining Ag-nanodots/Al reflective electrode with highly transparent p-type layer, *Opt Express* 29 (2) (2021) 2394–2401.
- [73] Y. Zhang, E.Z. Jamal, F. Akyol, S. Bajaj, J.M. Johnson, G. Calderon, et al., Tunnel-injected sub 290 nm ultra-violet light emitting diodes with 2.8% external quantum efficiency, *Appl. Phys. Lett.* 112 (7) (2018), 071107.
- [74] D. Zhang, C. Chu, K. Tian, J. Kou, W. Bi, Y. Zhang, et al., Improving hole injection from p-EBL down to the end of active region by simply playing with polarization effect for AlGaN based DUV light-emitting diodes, *AIP Adv.* 10 (6) (2020), 065032.
- [75] M.A. Khan, Y. Itokazu, N. Maeda, M. Jo, Y. Yamada, H. Hirayama, External quantum efficiency of 6.5% at 300 nm emission and 4.7% at 310 nm emission on bare wafer of AlGaN-based UVB LEDs, *ACS Appl. Electron Mater.* 2 (7) (2020) 1892–1907.
- [76] H. Yoshida, Y. Yamashita, M. Kuwabara, H. Kan, Demonstration of an ultraviolet 336 nm AlGaN multiple-quantum-well laser diode, *Appl. Phys. Lett.* 93 (24) (2008), 241106.
- [77] Z. Zhang, M. Kushimoto, T. Sakai, N. Sugiyama, L.J. Schowalter, C. Sasaoka, et al., A 271.8 nm deep-ultraviolet laser diode for room temperature operation, *APEX* 12 (12) (2019), 124003.
- [78] K. Sato, S. Yasue, K. Yamada, S. Tanaka, T. Omori, S. Ishizuka, et al., Room-temperature operation of AlGaN ultraviolet-B laser diode at 298 nm on lattice-relaxed Al_{0.6}Ga_{0.4}N/AlN/sapphire, *APEX* 13 (3) (2020), 031004.
- [79] J.L. Pau, E. Monroy, GaMA. Sánchez, E. Calleja, E. Muñoz, AlGaN ultraviolet photodetectors grown by molecular beam epitaxy on Si(111) substrates, *Mater. Sci. Eng. B* 93 (1) (2002) 159–162.
- [80] S. Nikishin, B. Borisov, M. Pandikunta, R. Dahal, J.Y. Lin, H.X. Jiang, et al., High quality AlN for deep UV photodetectors, *Appl. Phys. Lett.* 95 (5) (2009), 054101.
- [81] E. Ciciek, R. McClintock, C.Y. Cho, B. Rahnema, M. Razeghi, AlxGa1-xN-based back-illuminated solar-blind photodetectors with external quantum efficiency of 89%, *Appl. Phys. Lett.* 103 (19) (2013), 191108.
- [82] N. Biyikli, I. Kimukin, O. Aytur, E. Ozbay, Solar-blind AlGaN-based p-i-n photodiodes with low dark current and high detectivity, *IEEE Photon. Technol. Lett.* 16 (7) (2004) 1718–1720.
- [83] C.J. Collins, U. Chowdhury, M.M. Wong, B. Yang, A.L. Beck, R.D. Dupuis, et al., Improved solar-blind detectivity using an AlxGa1-xN heterojunction p-i-n photodiode, *Appl. Phys. Lett.* 80 (20) (2002) 3754–3756.
- [84] H. Chen, Y.R. Chen, H. Song, Z.M. Li, H. Jiang, D.B. Li, et al., Dependence of dark current and photoresponse on polarization charges for AlGaN-based heterojunction p-i-n photodetectors, *Phys. Status Solidi* 214 (6) (2017), 1600932.
- [85] R. Dahal, T.M. Al Tahtamouni, Z.Y. Fan, J.Y. Lin, H.X. Jiang, Hybrid AlN-SiC deep ultraviolet Schottky barrier photodetectors, *Appl. Phys. Lett.* 90 (26) (2007), 263505.
- [86] Z. Huang, J. Li, W. Zhang, H. Jiang, AlGaN solar-blind avalanche photodiodes with enhanced multiplication gain using back-illuminated structure, *APEX* 6 (5) (2013), 054101.
- [87] W. Zhang, J. Xu, W. Ye, Y. Li, Z. Qi, J. Dai, et al., High-performance AlGaN metal–semiconductor–metal solar-blind ultraviolet photodetectors by localized surface plasmon enhancement, *Appl. Phys. Lett.* 106 (2) (2015), 021112.
- [88] S. Rathkanthiwar, A. Kalra, S.V. Solanke, N. Mohta, R. Muralidharan, S. Raghavan, et al., Gain mechanism and carrier transport in high responsivity AlGaN-based solar blind metal semiconductor metal photodetectors, *J. Appl. Phys.* 121 (16) (2017), 164502.
- [89] L. Zhang, S. Tang, C. Liu, B. Li, H. Wu, H. Wang, et al., Demonstration of solar-blind AlxGa1-xN-based heterojunction phototransistors, *Appl. Phys. Lett.* 107 (23) (2015), 233501.
- [90] W. Zheng, R. Lin, J. Ran, Z. Zhang, X. Ji, F. Huang, Vacuum-ultraviolet photovoltaic detector, *ACS Nano* 12 (1) (2018) 425–431.
- [91] A. Kalra, S. Rathkanthiwar, R. Muralidharan, S. Raghavan, Polarization-graded AlGaN solar-blind p-i-n detector with 92% zero-bias external quantum efficiency, *IEEE Photon. Technol. Lett.* 31 (15) (2019) 1237–1240.
- [92] Y. Chen, Z. Zhang, G. Miao, H. Jiang, Z. Li, H. Song, Epitaxial growth of polarization-graded AlGaN-based solar-blind ultraviolet photodetectors on pre-grown AlN templates, *Mater. Lett.* 281 (2020), 128638.
- [93] P. Reddy, B.M. Hayden, Q. Guo, A. Klump, D. Khachariya, S. Pavlidis, et al., High gain, large area, and solar blind avalanche photodiodes based on Al-rich AlGaN grown on AlN substrates, *Appl. Phys. Lett.* 116 (8) (2020), 081101.
- [94] L. Hahn, F. Fuchs, L. Kirste, R. Driad, F. Rutz, T. Passow, et al., Avalanche multiplication in AlGaN-based heterostructures for the ultraviolet spectral range, *Appl. Phys. Lett.* 112 (15) (2018), 151102.
- [95] R. McClintock, A. Yasan, K. Minder, P. Kung, M. Razeghi, Avalanche multiplication in AlGaN based solar-blind photodetectors, *Appl. Phys. Lett.* 87 (24) (2005), 241123.
- [96] Z.G. Shao, X.F. Yang, H.F. You, D.J. Chen, H. Lu, R. Zhang, et al., Ionization-enhanced AlGaN heterostructure avalanche photodiodes, *IEEE Electron. Device Lett.* 38 (4) (2017) 485–488.
- [97] Q. Cai, Q. Li, M. Li, Y. Tang, J. Wang, J. Xue, et al., Performance modulation for back-illuminated AlGaN ultraviolet avalanche photodiodes based on multiplication scaling, *IEEE Photon J.* 11 (3) (2019) 1–7.
- [98] Q. Cai, W.K. Luo, Q. Li, M. Li, D.J. Chen, H. Lu, et al., AlGaN ultraviolet Avalanche photodiodes based on a triple-mesa structure, *Appl. Phys. Lett.* 113 (12) (2018), 123503.
- [99] D. Alden, J.S. Harris, Z. Bryan, J.N. Baker, P. Reddy, S. Mita, et al., Point-defect nature of the ultraviolet absorption band in AlN, *Phys. Rev. Appl.* 9 (5) (2018), 054036.
- [100] C. Hartmann, L. Matiwe, J. Wollweber, I. Gamov, K. Irmscher, M. Bickermann, et al., Favourable growth conditions for the preparation of bulk AlN single crystals by PVT, *CrystEngComm* 22 (10) (2020) 1762–1768.
- [101] R. Yu, G. Liu, G. Wang, C. Chen, M. Xu, H. Zhou, et al., Ultrawide-bandgap semiconductor AlN crystals: growth and applications, *J. Mater. Chem. C* 9 (6) (2021) 1852–1873.
- [102] S.V. Averine, P.I. Kuznetsov, V.A. Zhitov, N.V. Alkeev, Solar-blind MSM-photodetectors based on AlxGa1-xN/GaN heterostructures grown by MOCVD, *Solid State Electron.* 52 (5) (2008) 618–624.

- [103] M. Gökkavas, S. Butun, T. Tut, N. Biyikli, E. Ozbay, AlGaN-based high-performance metal–semiconductor–metal photodetectors, *Photonics Nanostruct.: Fundam Appl.* 5 (2) (2007) 53–62.
- [104] A. Knigge, M. Brendel, F. Brunner, S. Einfeldt, A. Knauer, V. Kueller, et al., AlGaN photodetectors for the UV-C spectral region on planar and epitaxial laterally overgrown AlN/sapphire templates, *Phys. Status Solidi C* 10 (3) (2013) 294–297.
- [105] K. Jiang, X. Sun, Z.H. Zhang, J. Ben, J. Che, Z. Shi, et al., Polarization-enhanced AlGaN solar-blind ultraviolet detectors, *Photon. Res.* 8 (7) (2020) 1243–1252.
- [106] A. Yoshikawa, S. Ushida, K. Nagase, M. Iwaya, T. Takeuchi, S. Kamiyama, et al., High-performance solar-blind Al_{0.6}Ga_{0.4}N/Al_{0.5}Ga_{0.5}N MSM type photodetector, *Appl. Phys. Lett.* 111 (19) (2017), 191103.
- [107] Q. Cai, H. You, H. Guo, J. Wang, B. Liu, Z. Xie, et al., Progress on AlGaN-based solar-blind ultraviolet photodetectors and focal plane arrays, *Light Sci. Appl.* 10 (1) (2021) 94.
- [108] A. Rogalski, Progress in focal plane array technologies, *Prog. Quant. Electron.* 36 (2) (2012) 342–473.
- [109] P. Lamarre, A. Hairston, S.P. Tobin, K.K. Wong, A.K. Sood, M.B. Reine, et al., AlGaN UV focal plane arrays, *Phys. Status Solidi* 188 (1) (2001) 289–292.
- [110] P.E. Malinowski, J. Duboz, M.P. De, J. John, K. Mingolou, P. Srivastava, et al., AlGaN-on-Si-Based 10-μm pixel-to-pixel pitch hybrid imagers for the EUV range, *IEEE Electron. Device Lett.* 32 (11) (2011) 1561–1563.
- [111] R. Rehm, R. Driad, L. Kirste, S. Leone, T. Passow, F. Rutz, et al., Toward AlGaN focal plane arrays for solar-blind ultraviolet detection, *Phys. Status Solidi* 217 (7) (2020), 1900769.
- [112] Y. Yuan, Y. Zhang, K. Chu, X. Li, D. Zhao, H. Yang, Development of solar-blind AlGaN 128×128 ultraviolet focal plane arrays, *Sci. China SeriesE: Technol. Sci.* 51 (6) (2008) 820–826.
- [113] Y. Zhang, J. Zhang, Z. Liu, S. Xu, K. Cheng, J. Ning, et al., Demonstration of a 2 kV Al_{0.85}Ga_{0.15}N Schottky barrier diode with improved on-current and ideality factor, *IEEE Electron. Device Lett.* 41 (3) (2020) 457–460.
- [114] H. Fu, J. Baranowski, X. Huang, I. Chen, Z. Lu, J. Montes, et al., Demonstration of AlN Schottky barrier diodes with blocking voltage over 1 kV, *IEEE Electron. Device Lett.* 38 (9) (2017) 1286–1289.
- [115] T. Zhang, J. Zhang, W. Zhang, Y. Zhang, X. Duan, J. Ning, et al., Investigation of an AlGaN-channel Schottky barrier diode on a silicon substrate with a molybdenum anode, *Semicond. Sci. Technol.* 36 (4) (2021), 044003.
- [116] J. Xie, S. Mia, R. Dalmau, R. Collazo, A. Rice, J. Tweedie, et al., In Ni/Au Schottky diodes on Al_xGa_{1-x}N (0.7 < x < 1) grown on AlN single crystal substrates, *Phys. Status Solidi C* 8 (7–8) (2011) 2407–2409.
- [117] T. Kinoshita, T. Nagashima, T. Obata, S. Takashima, R. Yamamoto, R. Togashi, et al., Fabrication of vertical Schottky barrier diodes on n-type freestanding AlN substrates grown by hydride vapor phase epitaxy, *APEX* 8 (6) (2015), 061003.
- [118] A.S.A. Fletcher, D. Nirmal, A survey of Gallium Nitride HEMT for RF and high power applications, *Superlattice. Microst.* 109 (2017) 519–537.
- [119] U.K. Mishra, P. Parikh, F.W. Yi, AlGaN/GaN HEMTs—an overview of device operation and applications, *Proc. IEEE* 90 (6) (2002) 1022–1031.
- [120] F. Roccaforte, P. Fiorenza, G. Greco, R. Lo Nigro, F. Giannazzo, F. Iucolano, et al., Emerging trends in wide band gap semiconductors (SiC and GaN) technology for power devices, *Microelectron. Eng.* 187–188 (2018) 66–77.
- [121] N. Yafune, S. Hashimoto, K. Akita, Y. Yamamoto, H. Tokuda, M. Kuzuhara, AlN/AlGaN HEMTs on AlN substrate for stable high-temperature operation, *Electron. Lett.* 50 (3) (2014) 211–212.
- [122] X. Hu, S. Hwang, K. Hussain, R. Floyd, S. Mollah, F. Asif, et al., Doped barrier Al_{0.6}Ga_{0.35}/Al_{0.4}Ga_{0.6}N MOSFET with SiO₂ gate-insulator and Zr-based ohmic contacts, *IEEE Electron. Device Lett.* 39 (10) (2018) 1568–1571.
- [123] H. Xue, K. Hussain, T. Razzak, M. Gaevski, S.H. Sohel, S. Mollah, et al., Al_{0.65}Ga_{0.35}/Al_{0.4}Ga_{0.6}N micro-channel heterojunction field effect transistors with current density over 900 mA/mm, *IEEE Electron. Device Lett.* 41 (5) (2020) 677–680.
- [124] M. Gaevski, S. Mollah, K. Hussain, J. Letton, A. Mamun, M.U. Jewel, et al., Ultrawide bandgap Al_xGa_{1-x}N channel heterostructure field transistors with drain currents exceeding 1.3 A mm⁻¹, *APEX* 13 (9) (2020), 094002.
- [125] B.A. Klein, E.A. Douglas, A.M. Armstrong, A.A. Allerman, V.M. Abate, T.R. Fortune, et al., Enhancement-mode Al_{0.85}Ga_{0.15}N/Al_{0.7}Ga_{0.3}N high electron mobility transistor with fluorine treatment, *Appl. Phys. Lett.* 114 (11) (2019), 112104.
- [126] E.A. Douglas, B. Klein, A.A. Allerman, A.G. Baca, T. Fortune, A.M. Armstrong, Enhancement-mode AlGaN channel high electron mobility transistor enabled by p-AlGaN gate, *J. Vac. Sci. Technol. B* 37 (2) (2019), 021208.
- [127] H. Xue, K. Hussain, V. Talesara, T. Razzak, M. Gaevski, S. Mollah, et al., High-current-density enhancement-mode ultrawide-bandgap AlGaN channel metal-insulator-semiconductor heterojunction field-effect transistors with a threshold voltage of 5 V, *Phys. Status Solidi Rapid Res. Lett.* 15 (6) (2021), 2000576.
- [128] S. Muhtadi, S. Hwang, A. Coleman, F. Asif, A. Lunev, M.V.S. Chandrashekhar, et al., High temperature operation of n-AlGaN channel metal semiconductor field effect transistors on low-defect AlN templates, *Appl. Phys. Lett.* 110 (19) (2017), 193501.
- [129] H. Okumura, S. Suikonen, J. Lemettinen, A. Uedono, Y. Zhang, D. Piedra, et al., AlN metal–semiconductor field-effect transistors using Si-ion implantation, *Jpn. J. Appl. Phys.* 57 (4S) (2018), 04FR11.
- [130] All MOCVD grown 250 nm gate length Al_{0.70}Ga_{0.30}N MESFETs, in: H. Xue, T. Razzak, J. Hwang, A. Coleman, S. Bajaj, Y. Zhang, et al. (Eds.), 2018 76th Device Research Conference (DRC); 2018 24–27 June, 2018.
- [131] H. Xue, C.H. Lee, K. Hussain, T. Razzak, M. Abdullah, Z. Xia, et al., Al_{0.75}Ga_{0.25}N/Al_{0.6}Ga_{0.4}N heterojunction field effect transistor with fT of 40 GHz, *APEX* 12 (6) (2019), 066502.
- [132] I. Akimoto, Y. Handa, K. Fukai, N. Naka, High carrier mobility in ultrapure diamond measured by time-resolved cyclotron resonance, *Appl. Phys. Lett.* 105 (3) (2014), 032102.
- [133] S.A. Linnik, S.P. Zenkin, A.V. Gaydaychuk, Heteroepitaxial diamond growth from the gas phase: problems and prospects (review), *Instrum. Exp. Tech.* 64 (2) (2021) 177–189.
- [134] S. Mandal, Nucleation of diamond films on heterogeneous substrates: a review, *RSC Adv.* 11 (17) (2021) 10159–10182.
- [135] K. Hayashi, S. Yamanaka, H. Watanabe, T. Sekiguchi, H. Okushi, K. Kajimura, Investigation of the effect of hydrogen on electrical and optical properties in chemical vapor deposited on homoepitaxial diamond films, *J. Appl. Phys.* 81 (2) (1997) 744–753.
- [136] S. Koizumi, M. Kamo, Y. Sato, H. Ozaki, T. Inuzuka, Growth and characterization of phosphorous doped {111} homoepitaxial diamond thin films, *Appl. Phys. Lett.* 71 (8) (1997) 1065–1067.
- [137] H. Yamada, A. Chayahara, Y. Mokuno, Y. Kato, S. Shikata, A 2-in. mosaic wafer made of a single-crystal diamond, *Appl. Phys. Lett.* 104 (10) (2014), 102110.
- [138] M. Schreck, S. Gsell, R. Brescia, M. Fischer, Ion bombardment induced buried lateral growth: the key mechanism for the synthesis of single crystal diamond wafers, *Sci. Rep.* 7 (1) (2017), 44462.
- [139] J.P. Lagrange, A. Deneuville, E. Gheeraert, Activation energy in low compensated homoepitaxial boron-doped diamond films Paper presented at the Diamond 1997 Conference, Diam. Relat. Mater. 7 (9) (1998) 1390–1393.
- [140] Y.J. Lu, C.N. Lin, C.X. Shan, Optoelectronic diamond: growth, properties, and photodetection applications, *Adv. Opt. Mater.* 6 (20) (2018), 1800359.
- [141] H. Kato, H. Umezawa, N. Tokuda, D. Takeuchi, H. Okushi, S. Yamasaki, Low specific contact resistance of heavily phosphorus-doped diamond film, *Appl. Phys. Lett.* 93 (20) (2008), 202103.
- [142] T. Matsumoto, H. Kato, T. Makino, M. Ogura, D. Takeuchi, H. Okushi, et al., Carrier transport in homoepitaxial diamond films with heavy phosphorus doping, *Jpn. J. Appl. Phys.* 53 (5S1) (2014), 05FP.
- [143] T.M.A. Pinault, S. Temgoua, R. Gillet, H. Bensalah, I. Stenger, F. Jomard, et al., Phosphorus-doped (113) CVD diamond: a breakthrough towards bipolar diamond devices, *Appl. Phys. Lett.* 114 (11) (2019), 112106.
- [144] C.N. Lin, Y.J. Lu, X. Yang, Y.Z. Tian, C.J. Gao, J.L. Sun, et al., Diamond-based all-carbon photodetectors for solar-blind imaging, *Adv. Opt. Mater.* 6 (15) (2018), 1800068.
- [145] K. Liu, B. Dai, V. Ralchenko, Y. Xia, B. Quan, J. Zhao, et al., Single crystal diamond UV detector with a groove-shaped electrode structure and enhanced sensitivity, *Sens. Actuator A Phys.* 259 (2017) 121–126.

- [146] Y.C. Chen, Y.J. Lu, C.N. Lin, Y.Z. Tian, C.J. Gao, L. Dong, et al., Self-powered diamond/ β -Ga₂O₃ photodetectors for solar-blind imaging, *J. Mater. Chem. C* 6 (21) (2018) 5727–5732.
- [147] Z. Liu, F. Lin, D. Zhao, T. Min, H. Wang, Fabrication and characterization of (100)-oriented single-crystal diamond p-i-n junction ultraviolet detector, *Phys. Status Solidi* 217 (21) (2020), 2000207.
- [148] M. Wei, K. Yao, Y. Liu, C. Yang, X. Zang, L. Lin, A solar-blind UV detector based on graphene-microcrystalline diamond heterojunctions, *Small* 13 (34) (2017), 1701328.
- [149] F.N. Li, Y. Li, D.Y. Fan, H.X. Wang, Self-powered diamond ultraviolet photodetector with a transparent Ag nanowire electrode, *Nanotechnology* 30 (32) (2019), 325204.
- [150] Z. Liu, D. Zhao, T. Min, J. Wang, G. Chen, H. Wang, Photovoltaic three-dimensional diamond UV photodetector with low dark current and fast response speed fabricated by bottom-up method, *IEEE Electron. Device Lett.* 40 (7) (2019) 1186–1189.
- [151] G. Prestopino, M. Marinelli, E. Milani, C. Verona, G. Verona-Rinati, Transient lateral photovoltaic effect in synthetic single crystal diamond, *Appl. Phys. Lett.* 111 (14) (2017), 143504.
- [152] X. Chang, Y.F. Wang, X. Zhang, Z. Liu, J. Fu, S. Fan, et al., UV-photodetector based on NiO/diamond film, *Appl. Phys. Lett.* 112 (3) (2018), 032103.
- [153] K. Liu, W. Wang, B. Dai, L. Yang, J. Zhao, J. Xue, et al., Impact of UV spot position on forward and reverse photocurrent symmetry in a gold-diamond-gold detector, *Appl. Phys. Lett.* 113 (2) (2018), 023501.
- [154] Z. Liu, D. Zhao, T. Zhu, J. Wang, W. Yi, T. Min, et al., Enhanced responsivity of diamond UV detector based on regrown lens structure, *IEEE Electron. Device Lett.* 41 (12) (2020) 1829–1832.
- [155] X. Chang, Y.F. Wang, X. Zhang, Z. Liu, J. Fu, D. Zhao, et al., Enhanced ultraviolet absorption in diamond surface via localized surface plasmon resonance in palladium nanoparticles, *Appl. Surf. Sci.* 464 (2019) 455–457.
- [156] X. Chang, Y.F. Wang, X. Zhang, R. Wang, Z. Liu, J. Fu, et al., Iridium size effects in localized surface plasmon-enhanced diamond UV photodetectors, *Appl. Surf. Sci.* 487 (2019) 674–677.
- [157] Z. Zhang, C. Lin, X. Yang, Y. Tian, C. Gao, K. Li, et al., Solar-blind imaging based on 2-inch polycrystalline diamond photodetector linear array, *Carbon* 173 (2021) 427–432.
- [158] Z. Liu, J.P. Ao, F. Li, W. Wang, J. Wang, J. Zhang, et al., Photoelectrical characteristics of ultra thin TiO₂/diamond photodetector, *Mater. Lett.* 188 (2017) 52–54.
- [159] Z. Liu, D. Zhao, J.P. Ao, W. Wang, X. Chang, Y. Wang, et al., Enhanced ultraviolet photoresponse of diamond photodetector using patterned diamond film and two-step growth process, *Mater. Sci. Semicond. Process.* 89 (2019) 110–115.
- [160] X. Chang, Y.F. Wang, H.N. Abbasi, R. Wang, Z. Liu, J. Wang, et al., Pd nanoparticle size effects in localized surface plasmon-enhanced diamond photodetectors, *Opt. Mater.* 107 (2020), 110031.
- [161] K. Liu, B. Liu, J. Zhao, G. Shu, X. Xu, K. Yao, et al., Application of back bias to interdigital-electrode structured diamond UV detector showing enhanced responsivity, *Sens. Actuator A Phys.* 290 (2019) 222–227.
- [162] Z. Liu, D. Zhao, J. Ao, X. Chang, Y. Wang, J. Fu, et al., Responsivity improvement of Ti-diamond-Ti structured UV photodetector through photocurrent gain, *Opt Express* 26 (13) (2018) 17092–17098.
- [163] C. Lin, Y. Lu, Y. Tian, C. Gao, M. Fan, X. Yang, et al., Diamond based photodetectors for solar-blind communication, *Opt Express* 27 (21) (2019) 29962–29971.
- [164] M. Suzuki, High voltage diamond pin diodes: feasibility study on ultimate properties of diamond toward ultimate power devices, *Oyo Buturi* 85 (2016) 218–222.
- [165] P.N. Volpe, P. Muret, J. Pernot, F. Omnès, T. Teraji, Y. Koide, et al., Extreme dielectric strength in boron doped homoepitaxial diamond, *Appl. Phys. Lett.* 97 (22) (2010), 223501.
- [166] T. Makino, H. Kato, N. Tokuda, M. Ogura, D. Takeuchi, K. Oyama, et al., Diamond Schottky-pn diode without trade-off relationship between on-resistance and blocking voltage, *Phys. Status Solidi* 207 (9) (2010) 2105–2109.
- [167] T. Makino, S. Tanimoto, Y. Hayashi, H. Kato, N. Tokuda, M. Ogura, et al., Diamond Schottky-pn diode with high forward current density and fast switching operation, *Appl. Phys. Lett.* 94 (26) (2009), 262101.
- [168] T. Iwasaki, H. Kato, T. Makino, M. Ogura, D. Takeuchi, S. Yamasaki, et al., High-temperature bipolar-mode operation of normally-off diamond JFET, *IEEE J. Electron Devices Soc.* 5 (1) (2017) 95–99.
- [169] T. Iwasaki, J. Yaita, H. Kato, T. Makino, M. Ogura, D. Takeuchi, et al., 600 V diamond junction field-effect transistors operated at 200 degrees C, *IEEE Electron. Device Lett.* 35 (2) (2014) 241–243.
- [170] H. Kato, T. Makino, M. Ogura, D. Takeuchi, S. Yamasaki, Fabrication of bipolar junction transistor on (001)-oriented diamond by utilizing phosphorus-doped n-type diamond base, *Diam. Relat. Mater.* 34 (2013) 41–44.
- [171] H. Kato, K. Oyama, T. Makino, M. Ogura, D. Takeuchi, S. Yamasaki, Diamond bipolar junction transistor device with phosphorus-doped diamond base layer, *Diam. Relat. Mater.* 27–28 (2012) 19–22.
- [172] K. Hirama, H. Sato, Y. Harada, H. Yamamoto, M. Kasu, Diamond field-effect transistors with 1.3A/mm drain current density by Al₂O₃ passivation layer, *Jpn. J. Appl. Phys.* 51 (2012), 090112.
- [173] N.C. Saha, S.W. Kim, T. Oishi, Y. Kawamata, K. Koyama, M. Kasu, 345-MW/cm² 2608-V NO₂ p-type doped diamond MOSFETs with an Al₂O₃ passivation overlayer on heteroepitaxial diamond, *IEEE Electron. Device Lett.* 42 (6) (2021) 903–906.
- [174] J. Tsunoda, M. Iwataki, K. Horikawa, S. Amano, K. Ota, A. Hiraiwa, et al., Low ON-resistance (2.5 m omega center dot cm(2)) vertical-type 2-D hole gas diamond MOSFETs with trench gate structure, *IEEE Trans. Electron. Dev.* 68 (7) (2021) 3490–3496.
- [175] Y. Kitabayashi, T. Kudo, H. Tsuboi, T. Yamada, D. Xu, M. Shibata, et al., Normally-off C-H diamond MOSFETs with partial C-O channel achieving 2-kV breakdown voltage, *IEEE Electron. Device Lett.* 38 (3) (2017) 363–366.
- [176] W. Wang, Y. Wang, M. Zhang, R. Wang, G. Chen, X. Chang, et al., An enhancement-mode hydrogen-terminated diamond field-effect transistor with lanthanum hexaboride gate material, *IEEE Electron. Device Lett.* 41 (4) (2020) 585–588.
- [177] M. Liao, L. Sang, T. Shimaoka, M. Imura, S. Koizumi, Y. Koide, Energy-efficient metal-insulator-metal-semiconductor field-effect transistors based on 2D carrier gases, *Adv. Electron. Mater.* 5 (5) (2019), 1800832.
- [178] M. Zhang, W. Wang, G. Chen, H.N. Abbasi, Y. Wang, F. Lin, et al., Normally OFF hydrogen-terminated diamond field-effect transistor with Ti/TiO_x gate materials, *IEEE Trans. Electron. Dev.* 67 (11) (2020) 4784–4788.
- [179] M. Zhang, W. Wang, S. Fan, G. Chen, H.N. Abbasi, F. Lin, et al., Normally-off hydrogen-terminated diamond field effect transistor with yttrium gate, *Carbon* 176 (2021) 307–312.
- [180] Z. Ren, Z. Liang, K. Su, Y. Xing, J. Zhang, J. Zhang, et al., Polycrystalline diamond normally-off MESFET passivated by a MoO₃ layer, *Results Phys.* 20 (2021), 103760.
- [181] Y.T. Lee, A. Vardi, M. Tordjman, A hybrid self-aligned MIS-MESFET architecture for improved diamond-based transistors, *Appl. Phys. Lett.* 117 (20) (2020), 202101.
- [182] J. Liu, T. Teraji, B. Da, Y. Koide, High output current boron-doped diamond metal-semiconductor field-effect transistors, *IEEE Electron. Device Lett.* 40 (11) (2019) 1748–1751.
- [183] C. De Santis, L. Pavanello, A. Nardo, C. Verona, G.V. Rinati, D. Cannatà, et al., Cause and effects of OFF-state degradation in hydrogen-terminated diamond MESFETs, *IEEE Trans. Electron. Dev.* 67 (10) (2020) 4021–4026.
- [184] M.I. Landstrass, K.V. Ravi, Hydrogen passivation of electrically active defects in diamond, *Appl. Phys. Lett.* 55 (14) (1989) 1391–1393.
- [185] E. Nebel Christoph, Surface-conducting diamond, *Science* 318 (5855) (2007) 1391–1392.
- [186] H. Umezawa, H. Taniuchi, T. Arima, M. Tachiki, H. Okushi, H. Kawarada (Eds.), High-performance Surface-Channel Diamond Field-Effect Transistors. Mater Sci Forum, Trans Tech Publications Ltd., Zurich-Uetikon, Switzerland, 2001.

- [187] K. Ueda, M. Kasu, Y. Yamauchi, T. Makimoto, M. Schwitters, Diamond FET using high-quality polycrystalline diamond with f(T) of 45 GHz and f(max) of 120 GHz, *IEEE Electron. Device Lett.* 27 (7) (2006) 570–572.
- [188] X. Yu, J. Zhou, C. Qi, Z. Cao, Y. Kong, T. Chen, A high frequency hydrogen-terminated diamond MISFET with f(T)/f(max) of 70/80 GHz, *IEEE Electron. Device Lett.* 39 (9) (2018) 1373–1376.
- [189] S. Imanishi, K. Horikawa, N. Oi, S. Okubo, T. Kageura, A. Hiraiwa, et al., 3.8W/mm RF power density for ALD Al2O3-based two-dimensional hole gas diamond MOSFET operating at saturation velocity, *IEEE Electron. Device Lett.* 40 (2) (2019) 279–282.
- [190] X. Yu, W. Hu, J. Zhou, B. Liu, T. Tao, Y. Kong, et al., 1 W/mm output power density for H-terminated diamond MOSFETs with Al2O3/SiO2 Bi-layer passivation at 2 GHz, *IEEE J. Electron. Devices Soc.* 9 (2021) 160–164.
- [191] C. Yu, C.J. Zhou, J.C. Guo, Z.Z. He, H.X. Wang, S.J. Cai, et al., 650 mW/mm output power density of H-terminated polycrystalline diamond MISFET at 10 GHz, *Electron. Lett.* 56 (7) (2020) 334–335.
- [192] S.J. Pearson, J. Yang, P.H. Cary, F. Ren, J. Kim, M.J. Tadjer, et al., A review of Ga2O3 materials, processing, and devices, *Appl. Phys. Rev.* 5 (1) (2018), 011301.
- [193] D. Guo, Q. Guo, Z. Chen, Z. Wu, P. Li, W. Tang, Review of Ga2O3-based optoelectronic devices, *Mater. Today Phys.* 11 (2019), 100157.
- [194] Z. Galazka, R. Uecker, D. Klimm, K. Irmscher, M. Naumann, M. Pietsch, et al., Scaling-up of bulk β -Ga2O3Single crystals by the Czochralski method, *ECS J. Solid State Sci. Technol.* 6 (2) (2016) Q3007–Q3011.
- [195] K. Hoshikawa, E. Ohba, T. Kobayashi, J. Yanagisawa, C. Miyagawa, Y. Nakamura, Growth of β -Ga2O3 single crystals using vertical Bridgman method in ambient air, *J. Cryst. Growth* 447 (2016) 36–41.
- [196] W. Mu, Z. Jia, Y. Yin, Q. Hu, Y. Li, B. Wu, et al., High quality crystal growth and anisotropic physical characterization of β -Ga2O3 single crystals grown by EFG method, *J. Alloys Compd.* 714 (2017) 453–458.
- [197] H. Zhou, L. Cong, J. Ma, B. Li, M. Chen, H. Xu, et al., High gain broadband photoconductor based on amorphous Ga2O3 and suppression of persistent photoconductivity, *J. Mater. Chem. C* 7 (42) (2019) 13149–13155.
- [198] X. Chen, W. Mu, Y. Xu, B. Fu, Z. Jia, F.-F. Ren, et al., Highly narrow-band polarization-sensitive solar-blind photodetectors based on β -Ga2O3 single crystals, *ACS Appl. Mater. Interfaces* 11 (7) (2019) 7131–7137.
- [199] Y.P. Qian, D.Y. Guo, X.L. Chu, H.Z. Shi, W.K. Zhu, K. Wang, et al., Mg-doped p-type β -Ga2O3 thin film for solar-blind ultraviolet photodetector, *Mater. Lett.* 209 (2017) 558–561.
- [200] Z.X. Jiang, Z.Y. Wu, C.C. Ma, J.N. Deng, H. Zhang, Y. Xu, et al., P-type β -Ga2O3 metal-semiconductor-metal solar-blind photodetectors with extremely high responsivity and gain-bandwidth product, *Mater. Today Phys.* 14 (2020), 100226.
- [201] X. Chen, Y. Xu, D. Zhou, S. Yang, F-f Ren, H. Lu, et al., Solar-blind photodetector with high avalanche gains and bias-tunable detecting functionality based on metastable phase α -Ga2O3/ZnO isotype heterostructures, *ACS Appl. Mater. Interfaces* 9 (42) (2017) 36997–37005.
- [202] P. Li, H. Shi, K. Chen, D. Guo, W. Cui, Y. Zhi, et al., Construction of GaN/Ga2O3 p-n junction for an extremely high responsivity self-powered UV photodetector, *J. Mater. Chem. C* 5 (40) (2017) 10562–10570.
- [203] X.C. Guo, N.H. Hao, D.Y. Guo, Z.P. Wu, Y.H. An, X.L. Chu, et al., β -Ga2O3/p-Si heterojunction solar-blind ultraviolet photodetector with enhanced photoelectric responsivity, *J. Alloys Compd.* 660 (2016) 136–140.
- [204] D. Guo, H. Liu, P. Li, Z. Wu, S. Wang, C. Cui, et al., Zero-power-consumption solar-blind photodetector based on β -Ga2O3/NSTO heterojunction, *ACS Appl. Mater. Interfaces* 9 (2) (2017) 1619–1628.
- [205] Z. Li, Y. Cheng, Y. Xu, Z. Hu, W. Zhi, D. Chen, et al., High-performance beta-Ga2O3 solar-blind Schottky barrier photodiode with record detectivity and ultrahigh gain via carrier multiplication process, *IEEE Electron. Device Lett.* 41 (12) (2020) 1794–1797.
- [206] K. Arora, N. Goel, M. Kumar, M. Kumar, Ultrahigh performance of self-powered β -Ga2O3 thin film solar-blind photodetector grown on cost-effective Si substrate using high-temperature seed layer, *ACS Photonics* 5 (6) (2018) 2391–2401.
- [207] B. Qiao, Z. Zhang, X. Xie, B. Li, K. Li, X. Chen, et al., Avalanche gain in metal–semiconductor–metal Ga2O3 solar-blind photodiodes, *J. Phys. Chem. C* 123 (30) (2019) 18516–18520.
- [208] Y. Qin, L. Li, X. Zhao, G.S. Tompa, H. Dong, G. Jian, et al., Metal–semiconductor–metal ϵ -Ga2O3 solar-blind photodetectors with a record-high responsivity rejection ratio and their gain mechanism, *ACS Photonics* 7 (3) (2020) 812–820.
- [209] X. Hou, H. Sun, S. Long, G.S. Tompa, T. Salagaj, Y. Qin, et al., Ultrahigh-performance solar-blind photodetector based on alpha-phase-dominated Ga2O3 film with record low dark current of 81 fA, *IEEE Electron. Device Lett.* 40 (9) (2019) 1483–1486.
- [210] C. Zhou, K. Liu, X. Chen, J. Feng, J. Yang, Z. Zhang, et al., Performance improvement of amorphous Ga2O3 ultraviolet photodetector by annealing under oxygen atmosphere, *J. Alloys Compd.* 840 (2020), 155585.
- [211] Y. Peng, Y. Zhang, Z. Chen, D. Guo, X. Zhang, P. Li, Arrays of solar-blind ultraviolet photodetector based on beta-Ga2O3 epitaxial thin films, *IEEE Photon. Technol. Lett.* 30 (11) (2018) 993–996.
- [212] Y. Chen, Y. Lu, M. Liao, Y. Tian, Q. Liu, C. Gao, et al., 3D solar-blind Ga2O3 photodetector array realized via origami method, *Adv. Electron Mater.* 29 (50) (2019), 1906040.
- [213] Y.C. Chen, Y.J. Lu, Q. Liu, C.N. Lin, J. Guo, J.H. Zang, et al., Ga2O3 photodetector arrays for solar-blind imaging, *J. Mater. Chem. C* 7 (9) (2019) 2557–2562.
- [214] C. Xie, X. Lu, Y. Liang, H. Chen, L. Wang, C. Wu, et al., Patterned growth of β -Ga2O3 thin films for solar-blind deep-ultraviolet photodetectors array and optical imaging application, *J. Mater. Sci. Technol.* 72 (2021) 189–196.
- [215] B. Qiao, Z. Zhang, X. Xie, B. Li, X. Chen, H. Zhao, et al., Quenching of persistent photocurrent in an oxide UV photodetector, *J. Mater. Chem. C* 9 (11) (2021) 4039–4045.
- [216] Y. Qin, S. Long, Q. He, H. Dong, G. Jian, Y. Zhang, et al., Amorphous gallium oxide-based gate-tunable high-performance thin film phototransistor for solar-blind imaging, *Adv. Electron Mater.* 5 (7) (2019), 1900389.
- [217] Z. Han, H. Liang, W. Huo, X. Zhu, X. Du, Z. Mei, Boosted UV photodetection performance in chemically etched amorphous Ga2O3 thin-film transistors, *Adv. Opt. Mater.* 8 (8) (2020), 1901833.
- [218] Y. Liu, L. Du, G. Liang, W. Mu, Z. Jia, M. Xu, et al., Ga2O3 field-effect-transistor-based solar-blind photodetector with fast response and high photo-to-dark current ratio, *IEEE Electron. Device Lett.* 39 (11) (2018) 1696–1699.
- [219] Y. Qin, H. Dong, S. Long, Q. He, G. Jian, Y. Zhang, et al., Enhancement-mode beta-Ga2O3 metal-oxide-semiconductor field-effect solar-blind phototransistor with ultrahigh detectivity and photo-to-dark current ratio, *IEEE Electron. Device Lett.* 40 (5) (2019) 742–745.
- [220] S. Oh, Y. Jung, M.A. Mastro, J.K. Hite, C.R. Eddy, J. Kim, Development of solar-blind photodetectors based on Si-implanted beta-Ga2O3, *Opt Express* 23 (22) (2015) 28300–28305.
- [221] X. Chen, K. Liu, Z. Zhang, C. Wang, B. Li, H. Zhao, et al., Self-powered solar-blind photodetector with fast response based on Au/ β -Ga2O3 nanowires array film Schottky junction, *ACS Appl. Mater. Interfaces* 8 (6) (2016) 4185–4191.
- [222] A.S. Pratipush, Z. Xia, S. Kumar, Y. Zhang, C. Joishi, R. Muralidharan, et al., MBE-grown beta-Ga2O3-based Schottky UV-C photodetectors with rectification ratio similar to 10(7), *IEEE Photon. Technol. Lett.* 30 (23) (2018) 2025–2028.
- [223] C. Hou, R.M. Gazoni, R.J. Reeves, M.W. Allen, High-temperature beta-Ga2O3 Schottky diodes and UVC photodetectors using RuOx contacts, *IEEE Electron. Device Lett.* 40 (10) (2019) 1587–1590.
- [224] T. Zhang, Y. Shen, Q. Feng, X. Tian, Y. Cai, Z. Hu, et al., The investigation of hybrid PEDOT:PSS/ β -Ga2O3 deep ultraviolet Schottky barrier photodetectors, *Nanoscale Res. Lett.* 15 (1) (2020) 163.
- [225] L. Shi, K. Chen, A. Zhai, G. Li, M. Fan, Y. Hao, et al., Status and outlook of metal–inorganic semiconductor–metal photodetectors, *Laser Photon. Rev.* 15 (1) (2021), 2000401.
- [226] S. Cui, Z. Mei, Y. Zhang, H. Liang, X. Du, Room-temperature fabricated amorphous Ga2O3 high-response-speed solar-blind photodetector on rigid and flexible substrates, *Adv. Opt. Mater.* 5 (19) (2017), 1700454.
- [227] Y. Qin, H. Sun, S. Long, G.S. Tompa, T. Salagaj, H. Dong, et al., High-performance metal-organic chemical vapor deposition grown epsilon-Ga2O3 solar-blind photodetector with asymmetric Schottky electrodes, *IEEE Electron. Device Lett.* 40 (9) (2019) 1475–1478.

- [228] Z. Hu, H. Zhou, Q. Feng, J. Zhang, C. Zhang, K. Dang, et al., Field-plated lateral beta-Ga₂O₃ Schottky barrie diode with high reverse blocking voltage of more than 3 kV and high DC power figure-of-merit of 500 MW/cm(2), IEEE Electron. Device Lett. 39 (10) (2018) 1564–1567.
- [229] C. Wang, H. Gong, W. Lei, Y. Cai, Z. Hu, S. Xu, et al., Demonstration of the p-NiO_x/n-Ga₂O₃ heterojunction gate FETs and diodes with BV2/R-on,R-sp figures of merit of 0.39 GW/cm(2) and 1.38 GW/cm(2), IEEE Electron. Device Lett. 42 (4) (2021) 485–488.
- [230] J. Yang, S. Ahn, F. Ren, S.J. Pearton, S. Jang, J. Kim, et al., High reverse breakdown voltage Schottky rectifiers without edge termination on Ga₂O₃, Appl. Phys. Lett. 110 (19) (2017), 192101.
- [231] S. Sharma, K. Zeng, S. Saha, U. Singisetti, Field-plated lateral Ga₂O₃ MOSFETs with polymer passivation and 8.03 kV breakdown voltage, IEEE Electron. Device Lett. 41 (6) (2020) 836–839.
- [232] Y. Zhang, C. Joishi, Z. Xia, M. Brenner, S. Lodha, S. Rajan, Demonstration of β -(Al_xGa_{1-x})₂O₃/Ga₂O₃ double heterostructure field effect transistors, Appl. Phys. Lett. 112 (23) (2018), 233503.
- [233] N. Moser, J. McCandless, A. Crespo, K. Leedy, A. Green, A. Neal, et al., Ge-Doped beta-Ga₂O₃ MOSFETs, IEEE Electron. Device Lett. 38 (6) (2017) 775–778.
- [234] K. Tetzner, T.E. Bahat, O. Hilt, A. Popp, A.S. Bin, G. Wagner, et al., Lateral 1.8 kV beta-Ga₂O₃ MOSFET with 155 MW/cm(2) power figure of merit, IEEE Electron. Device Lett. 40 (9) (2019) 1503–1506.
- [235] Y. Lv, H. Liu, X. Zhou, Y. Wang, X. Song, Y. Cai, et al., Lateral beta-Ga₂O₃ MOSFETs with high power figure of merit of 277 MW/cm(2), IEEE Electron. Device Lett. 41 (4) (2020) 537–540.
- [236] Y. Lv, X. Zhou, S. Long, Y. Wang, X. Song, X. Zhou, et al., Enhancement-mode β -Ga₂O₃ metal-oxide-semiconductor field-effect transistor with high breakdown voltage over 3000 V realized by oxygen annealing, Phys. Status Solidi Rapid Res. Lett. 14 (3) (2020), 1900586.
- [237] Z. Hu, K. Nomoto, W. Li, N. Tanen, K. Sasaki, A. Kuramata, et al., Enhancement-mode Ga₂O₃ vertical transistors with breakdown voltage > 1 kV, IEEE Electron. Device Lett. 39 (6) (2018) 869–872.
- [238] W. Li, K. Nomoto, Z. Hu, T. Nakamura, D. Jena, H.G. Xing (Eds.), Single and Multi-Fin Normally-Off Ga₂O₃ Vertical Transistors with a Breakdown Voltage over 2.6 kV. 2019 IEEE International Electron Devices Meeting (IEDM); 2019 7–11 Dec, 2019.
- [239] N.K. Kalarickal, Z. Xia, H.L. Huang, W. Moore, Y. Liu, M. Brenner, et al., beta-(Al_{0.18}Ga_{0.82})₂O₃/Ga₂O₃ double heterojunction transistor with average field of 5.5 MV/cm, IEEE Electron. Device Lett. 42 (6) (2021) 899–902.
- [240] H. Zhang, L. Yuan, X. Tang, J. Hu, J. Sun, Y. Zhang, et al., Progress of ultra-wide bandgap Ga₂O₃ semiconductor materials in power MOSFETs, IEEE Trans. Power Electron. 35 (5) (2020) 5157–5179.
- [241] H. Dong, H. Xue, Q. He, Y. Qin, G. Jian, S. Long, et al., Progress of power field effect transistor based on ultra-wide bandgap Ga₂O₃ semiconductor material, J. Semiconduct. 40 (1) (2019), 011802.
- [242] K. Zeng, A. Vaidya, U. Singisetti, 1.85 kV breakdown voltage in lateral field-plated Ga₂O₃ MOSFETs, IEEE Electron. Device Lett. 39 (9) (2018) 1385–1388.
- [243] K.D. Chabak, N. Moser, A.J. Green, D.E. Walker, S.E. Tetlak, E. Heller, et al., Enhancement-mode Ga₂O₃ wrap-gate fin field-effect transistors on native (100) β -Ga₂O₃ substrate with high breakdown voltage, Appl. Phys. Lett. 109 (21) (2016), 213501.
- [244] S. Krishnamoorthy, Z. Xia, C. Joishi, Y. Zhang, J. McGlone, J. Johnson, et al., Modulation-doped β -(Al_{0.2}Ga_{0.8})₂O₃/Ga₂O₃ field-effect transistor, Appl. Phys. Lett. 111 (2) (2017), 023502.
- [245] H. Zhou, K. Maize, G. Qiu, A. Shakouri, P.D. Ye, β -Ga₂O₃ on insulator field-effect transistors with drain currents exceeding 1.5 A/mm and their self-heating effect, Appl. Phys. Lett. 111 (9) (2017), 092102.
- [246] Z. Hu, K. Nomoto, W. Li, Z. Zhang, N. Tanen, Q.T. Thieu, et al., Breakdown mechanism in 1 kA/cm² and 960 V E-mode β -Ga₂O₃ vertical transistors, Appl. Phys. Lett. 113 (12) (2018), 122103.
- [247] H. Zhou, M. Si, S. Alghamdi, G. Qiu, L. Yang, P.D. Ye, High-performance depletion/enhancement-mode \$ β \$-Ga₂O₃ on insulator (GOOI) field-effect transistors with record drain currents of 600/450 mA/mm, IEEE Electron. Device Lett. 38 (1) (2017) 103–106.
- [248] M. Xiao, B. Wang, J. Liu, R. Zhang, Z. Zhang, C. Ding, et al., Packaged Ga₂O₃ Schottky rectifiers with over 60-A surge current capability, IEEE Trans. Power Electron. 36 (8) (2021) 8565–8569.
- [249] K.D. Chabak, J.P. McCandless, N.A. Moser, A.J. Green, K. Mahalingam, A. Crespo, et al., Recessed-gate enhancement-mode \$ β \$-Ga₂O₃ MOSFETs, IEEE Electron. Device Lett. 39 (1) (2018) 67–70.
- [250] Y. Kokubun, S. Kubo, S. Nakagomi, All-oxide p-n heterojunction diodes comprising p-type NiO and n-type β -Ga₂O₃, APEX 9 (9) (2016), 091101.
- [251] S. Ghosh, M. Baral, R. Kamparath, S.D. Singh, T. Ganguli, Investigations on band commutativity at all oxide p-type NiO/n-type β -Ga₂O₃ heterojunction using photoelectron spectroscopy, Appl. Phys. Lett. 115 (25) (2019), 251603.
- [252] H.H. Gong, X.H. Chen, Y. Xu, F.F. Ren, S.L. Gu, J.D. Ye, A 1.86-kV double-layered NiO/ β -Ga₂O₃ vertical p-n heterojunction diode, Appl. Phys. Lett. 117 (2) (2020), 022104.
- [253] X. Lu, X. Zhou, H. Jiang, K.W. Ng, Z. Chen, Y. Pei, et al., 1-kV sputtered p-NiO/n-Ga₂O₃ heterojunction diodes with an ultra-low leakage current below 1 mu A/cm², IEEE Electron. Device Lett. 41 (3) (2020) 449–452.
- [254] T. Watahiki, Y. Yuda, A. Furukawa, M. Yamamuka, Y. Takiguchi, S. Miyajima, Heterojunction p-Cu₂O/n-Ga₂O₃ diode with high breakdown voltage, Appl. Phys. Lett. 111 (22) (2017), 222104.
- [255] Y. Zhang, T. Palacios, (Ultra)Wide-Bandgap vertical power FinFETs, IEEE Trans. Electron. Dev. 67 (10) (2020) 3960–3971.
- [256] A.J. Green, K.D. Chabak, M. Baldini, N. Moser, R. Gilbert, R.C. Fitch, et al., beta-Ga₂O₃ MOSFETs for radio frequency operation, IEEE Electron. Device Lett. 38 (6) (2017) 790–793.
- [257] Z. Xia, H. Xue, C. Joishi, J. McGlone, N.K. Kalarickal, M. Brenner, beta-Ga₂O₃ delta-doped field-effect transistors with current gain cutoff frequency of 27 GHz, IEEE Electron. Device Lett. 40 (7) (2019) 1052–1055.
- [258] N.A. Moser, T. Asel, K.J. Liddy, M. Lindquist, N.C. Miller, S. Mou, et al., Pulsed power performance of beta-Ga₂O₃ MOSFETs at L-band, IEEE Electron. Device Lett. 41 (7) (2020) 989–992.
- [259] Y. Lv, H. Liu, Y. Wang, X. Fu, C. Ma, X. Song, et al., Oxygen annealing impact on β -Ga₂O₃ MOSFETs: improved pinch-off characteristic and output power density, Appl. Phys. Lett. 117 (13) (2020), 133503.
- [260] D.C. Look, K.D. Leedy, R.H. Horng, M.D. Santia, S.C. Badescu, Electrical and optical properties of degenerate and semi-insulating ZnGa₂O₄: electron/phonon scattering elucidated by quantum magnetoconductivity, Appl. Phys. Lett. 116 (25) (2020), 252104.
- [261] L. Li, Y. Wang, H. Li, H. Huang, H. Zhao, Suppression of photocatalysis and long-lasting luminescence in ZnGa₂O₄ by Cr³⁺ doping, RSC Adv. 5 (70) (2015) 57193–57200.
- [262] T. Ohtake, N. Sonoyama, T. Sakata, Photoluminescence dependence on imposing bias for ZnGa₂O₄ and ZnGa₂O₄ activated with Mn²⁺ or Cr³⁺ n-type semiconductor electrodes, Electrochim. Commun. 7 (12) (2005) 1389–1392.
- [263] S.S. Yi, J.S. Bae, B.K. Moon, J.H. Jeong, J.H. Kim, Photoluminescence characteristics of Se-doped ZnGa₂O₄:Mn²⁺ thin-film phosphors grown by pulsed laser deposition on Al₂O₃(0001) substrates, Appl. Phys. A 81 (6) (2005) 1325–1328.
- [264] M. Baojun, L. Keying, S. Weiguang, L. Wanji, One-pot synthesis of ZnO/ZnGa₂O₄ heterojunction with X/XY structure for improved photocatalytic activity, Appl. Surf. Sci. 317 (2014) 682–687.
- [265] X. Bai, X. Zhao, W. Fan, Preparation and enhanced photocatalytic hydrogen-evolution activity of ZnGa₂O₄/N-rGO heterostructures, RSC Adv. 7 (84) (2017) 53145–53156.
- [266] K. Ikarashi, J. Sato, H. Kobayashi, N. Saito, H. Nishiyama, Y. Inoue, Photocatalysis for water decomposition by RuO₂-dispersed ZnGa₂O₄ with d10 configuration, J. Phys. Chem. B 106 (35) (2002) 9048–9053.
- [267] S.Z. Karazhanov, P. Ravindran, Ab initio study of double oxides ZnX₂O₄ (X=Al, Ga, in) having spinel structure, J. Am. Ceram. Soc. 93 (10) (2010) 3335–3341.
- [268] Z. Galazka, S. Ganschow, R. Schewski, K. Irmscher, D. Klimm, A. Kwasniewski, et al., Ultra-wide bandgap, conductive, high mobility, and high quality melt-grown bulk ZnGa₂O₄ single crystals, Apl. Mater. 7 (2) (2018), 022512.
- [269] T.R. Paudel, A. Zukatayev, S. Lany, M. d'Avezac, A. Zunger, Doping rules and doping prototypes in A₂BO₄ spinel oxides, Adv. Electron Mater. 21 (23) (2011) 4493–4501.

- [270] E. Chikoidze, C. Sartel, I. Madaci, H. Mohamed, C. Vilar, B. Ballesteros, et al., p-Type ultrawide-band-gap spinel ZnGa₂O₄: new perspectives for energy electronics, *Cryst. Growth Des.* 20 (4) (2020) 2535–2546.
- [271] S.H. Tsai, S. Basu, C.Y. Huang, L.C. Hsu, Y.G. Lin, R.H. Horng, Deep-ultraviolet photodetectors based on epitaxial ZnGa₂O₄ thin films, *Sci. Rep.* 8 (1) (2018) 14056.
- [272] D. Han, K. Liu, Q. Hou, X. Chen, J. Yang, B. Li, et al., Self-powered solar-blind ZnGa₂O₄ UV photodetector with ultra-fast response speed, *Sens. Actuator A Phys.* 315 (2020), 112354.
- [273] D. Han, K. Liu, X. Chen, B. Li, T. Zhai, L. Liu, et al., Performance enhancement of a self-powered solar-blind UV photodetector based on ZnGa₂O₄/Si heterojunction via interface pyroelectric effect, *Appl. Phys. Lett.* 118 (25) (2021), 251101.
- [274] D. Han, K. Liu, J. Yang, X. Chen, B. Li, L. Liu, et al., Performance enhancement of a p-Si/n-ZnGa₂O₄ heterojunction solar-blind UV photodetector through interface engineering, *J. Mater. Chem. C* 9 (31) (2021) 10013–10019.
- [275] P.W. Chen, S.Y. Huang, S.H. Yuan, Y.A. Chen, P.W. Hsiao, D.S. Wuu, Quasi-single-crystalline ZnGa₂O₄ films via solid phase epitaxy for enhancing deep-ultraviolet photoresponse, *Adv. Mater. Interfac.* 6 (18) (2019), 1901075.
- [276] Y.C. Shen, C.Y. Tung, C.Y. Huang, Ya Lin, Y.G. Lin, R.H. Horng, Study on optoelectronic characteristics of ZnGa₂O₄ thin-film phototransistors, *ACS Appl. Electron Mater.* 1 (5) (2019) 783–788.
- [277] S.H. Tsai, Y.C. Shen, C.Y. Huang, R.H. Horng, Deep-ultraviolet Schottky photodetectors with high deep-ultraviolet/visible rejection based on a ZnGa₂O₄ thin film, *Appl. Surf. Sci.* 496 (2019), 143670.
- [278] P.H. Huang, Y.C. Shen, C.Y. Tung, C.Y. Huang, C.S. Tan, R.H. Horng, Energy-saving ZnGa₂O₄ phototransistor improved by thermal annealing, *ACS Appl. Electron Mater.* 2 (11) (2020) 3515–3521.
- [279] W. Lin, D. Zhang, S. Liu, Y. Li, W. Zheng, F. Huang, ZnGa₂O₄ deep-ultraviolet photodetector based on Si substrate, *Mater. Lett.* 283 (2021), 128805.
- [280] J.L. Yang, K.W. Liu, D.Z. Shen, Recent progress of ZnMgO ultraviolet photodetector, *Chin. Phys. B* 26 (4) (2017), 047308.
- [281] K. Liu, M. Sakurai, M. Aono, ZnO-based ultraviolet photodetectors, *Sensors* 10 (9) (2010).
- [282] Z.L. Liu, Z.X. Mei, T.C. Zhang, Y.P. Liu, Y. Guo, X.L. Du, et al., Solar-blind 4.55eV band gap Mg_{0.55}Zn_{0.45}O components fabricated using quasi-homo buffers, *J. Cryst. Growth* 311 (18) (2009) 4356–4359.
- [283] H.L. Liang, Z.X. Mei, Z.L. Liu, Y. Guo, A.Y. Azarov, A.Y. Kuznetsov, et al., Growth of single-phase Mg_{0.3}Zn_{0.7}O films suitable for solar-blind optical devices on RS-MgO substrates, *Thin Solid Films* 520 (6) (2012) 1705–1708.
- [284] C.Y.J. Lu, T. Yan, L. Chang, K.H. Ploog, M.M.C. Chou, C.M. Chiang, Rock-salt Zn_{1-x}Mg_xO epilayer having high Zn content grown on MgO (100) substrate by plasma-assisted molecular beam epitaxy, *J. Cryst. Growth* 378 (2013) 168–171.
- [285] C.X. Shan, J.S. Liu, Y.J. Lu, B.H. Li, F.C.C. Ling, D.Z. Shen, p-type doping of MgZnO films and their applications in optoelectronic devices, *Opt Lett.* 40 (13) (2015) 3041–3044.
- [286] V.S. Winston, W. Ming, R.C. Boutwell, L. Huiyong (Eds.), High Response Solar-Blind MgZnO Photodetectors Grown by Molecular Beam Epitaxy, ProcSPIE, 2014.
- [287] M.M. Fan, K.W. Liu, X. Chen, Z.Z. Zhang, B.H. Li, H.F. Zhao, et al., Realization of cubic ZnMgO photodetectors for UVB applications, *J. Mater. Chem. C* 3 (2) (2015) 313–317.
- [288] X. Xie, Z. Zhang, B. Li, S. Wang, D. Shen, Ultra-low threshold avalanche gain from solar-blind photodetector based on graded-band-gap-cubic-MgZnO, *Opt Express* 23 (25) (2015) 32329–32336.
- [289] M.M. Fan, K.W. Liu, X. Chen, X. Wang, Z.Z. Zhang, B.H. Li, et al., Mechanism of excellent photoelectric characteristics in mixed-phase ZnMgO ultraviolet photodetectors with single cutoff wavelength, *ACS Appl. Mater. Interfaces* 7 (37) (2015) 20600–20606.
- [290] M.M. Fan, K.W. Liu, Z.Z. Zhang, B.H. Li, X. Chen, D.X. Zhao, et al., High-performance solar-blind ultraviolet photodetector based on mixed-phase ZnMgO thin film, *Appl. Phys. Lett.* 105 (1) (2014), 011117.
- [291] S. Han, S.M. Liu, Y.M. Lu, P.J. Cao, W.J. Liu, Y.X. Zeng, et al., High performance solar-blind ultraviolet photo detector based on mixed-phase MgZnO thin film with different interfaces deposited by PLD method, *J. Alloys Compd.* 694 (2017) 168–174.
- [292] C. Zhou, K. Liu, Y. Zhu, J. Yang, X. Chen, B. Li, et al., Self-powered solar-blind ultraviolet photodetector based on Au/ZnMgO/ZnO:Al with comb-shaped Schottky electrode, *Sens. Actuator A Phys.* 295 (2019) 623–628.
- [293] X. Chen, L. Wang, K. Liu, Z. Zhang, B. Li, J. Wu, et al., Responsivity improvement of a packaged ZnMgO solar blind ultraviolet photodetector via a sealing treatment of silica gel, *J. Mater. Chem. C* 8 (3) (2020) 1089–1094.
- [294] W. Zhang, D. Jiang, Z. Guo, X. Yang, N. Hu, Y. Duan, et al., Controlling responsivity depends on change of interdigital electrodes in planar MgZnO UV photodetectors, *Superlattice. Microst.* 115 (2018) 177–182.
- [295] C.B. Samantaray, R.N. Singh, Review of synthesis and properties of cubic boron nitride (c-BN) thin films, *Int. Mater. Rev.* 50 (6) (2005) 313–344.
- [296] X.W. Zhang, Doping and electrical properties of cubic boron nitride thin films: a critical review, *Thin Solid Films* 544 (2013) 2–12.
- [297] A. Maity, S.J. Grenadier, J. Li, J.Y. Lin, H.X. Jiang, Hexagonal boron nitride: epitaxial growth and device applications, *Prog. Quant. Electron.* 76 (33) (2021).
- [298] J.D. Caldwell, I. Aharonovich, G. Cassabois, J.H. Edgar, B. Gil, D.N. Basov, Photonics with hexagonal boron nitride, *Nat. Rev. Mater.* 4 (8) (2019) 552–567.
- [299] L. Schué, L. Sponza, A. Plaud, H. Bensalah, K. Watanabe, T. Taniguchi, et al., Bright luminescence from indirect and strongly bound excitons in h-BN, *Phys. Rev. Lett.* 122 (6) (2019), 067401.
- [300] Y.R. Chen, Z.W. Zhang, H. Jiang, Z.M. Li, G.Q. Miao, H. Song, The optimized growth of AlN templates for back-illuminated AlGaN-based solar-blind ultraviolet photodetectors by MOCVD, *J. Mater. Chem. C* 6 (18) (2018) 4936–4942.
- [301] K.B. Nam, M.L. Nakarmi, J. Li, J.Y. Lin, H.X. Jiang, Mg acceptor level in AlN probed by deep ultraviolet photoluminescence, *Appl. Phys. Lett.* 83 (5) (2003) 878–880.
- [302] VdWG. Chris, J. Neugebauer, First-principles calculations for defects and impurities: applications to III-nitrides, *J. Appl. Phys.* 95 (8) (2004) 3851–3879.
- [303] A.F. Kohan, G. Ceder, D. Morgan, C.G. Van de Walle, First-principles study of native point defects in ZnO, *Phys. Rev. B* 61 (22) (2000) 15019–15027.
- [304] J. Simon, V. Protasenko, C. Lian, H. Xing, D. Jena, Polarization-induced hole doping in wide-band-gap uniaxial semiconductor heterostructures, *Science* 327 (5961) (2010) 60–64.
- [305] M.L. Nakarmi, K.H. Kim, J. Li, J.Y. Lin, H.X. Jiang, Enhanced p-type conduction in GaN and AlGaN by Mg-δ-doping, *Appl. Phys. Lett.* 82 (18) (2003) 3041–3043.
- [306] S. Koizumi, K. Watanabe, M. Hasegawa, H. Kanda, Ultraviolet emission from a diamond pn junction, *Science* 292 (5523) (2001) 1899–1901.